Title
Autonomous Surface Vehicle Measurement Location Planning for Optimal Underwater Acoustic Transponder Localization

Author
Garcia, Jesse R

Publication Date
2018

UNIVERSITY OF CALIFORNIA
RIVERSIDE

Autonomous Surface Vehicle Measurement Location Planning for Optimal Underwater Acoustic Transponder Localization

A Thesis submitted in partial satisfaction
of the requirements for the degree of

Master of Science

in

Electrical Engineering

by

Jesse R. Garcia

September 2018

Thesis Committee:

Professor Jay A. Farrell, Co-Chairperson
Professor Zaher (Zak) M. Kassas, Co-Chairperson
Dr. Michael T. Ouimet

The Thesis of Jesse R. Garcia is approved:

Committee Co-Chairperson

Committee Co-Chairperson

University of California, Riverside

Acknowledgments

The text of this thesis is a reprint of the material as it appears in [11] and [12]. Dr. Jay A. Farrell and Dr. Zaher (Zak) M. Kassas directed and supervised the research which forms the basis for this thesis, while Dr. Michael T. Ouimet provided technical expertise.

I thank my co-advisors at the University of California, Riverside (UCR) Jay A. Farrell and Zaher (Zak) M. Kassas, whose guidance and insight helped make this journey possible. I also thank my technical advisor T. Michael Ouimet at SPAWAR Systems Center (SSC) Pacific for the insight and friendship he has provided over the last two years.

I am very thankful to Maria Medeiros and Chris Duarte for believing in this research and providing two years of financial support through the Office of Naval Research's (ONR) Naval Undersea Research Program (NURP).

Thanks to Mike Tall, Tom Pastore, Tony Muñoz, Anthony Jones, and all other members of the HAMMER program at SSC Pacific for their technical expertise and help with experiments.

I thank my research colleagues both in Prof. Farrell's in Prof. Kassas' groups; Elahe Aghapour, Joe Khalife, and Joshua Morales for their many research and coursework discussions; Souradeep (Gogol) Bhattacharya, Sonya Ragothaman, and Kimia Shamaei for their constant friendship and reassurances; and Ali Abdallah, Christian Ardito, Madhi Mahreef, Farzana Rahman, and Kyle Semelka.

Special thanks to my friends that have challenged me and helped me grow outside of academia. I cannot express my gratitude to you enough; you know who you are.

To my parents, Frank and Bobbi, and my brother Jovanni.

ABSTRACT OF THE THESIS

Autonomous Surface Vehicle Measurement Location Planning for
Optimal Underwater Acoustic Transponder Localization

by

Jesse R. Garcia

Master of Science, Graduate Program in Electrical Engineering
University of California, Riverside, September 2018
Professor Jay A. Farrell, Co-Chairperson
Professor Zaher (Zak) M. Kassas, Co-Chairperson

The problem of an autonomous surface vehicle (ASV) optimally planning measurement locations to localize a set of pre-deployed acoustic underwater transponders (UTs) is considered. The ASV is assumed to make noisy range measurements to the UTs. A maximum *a posteriori* estimator is derived to localize the UTs. In addition, a multi-step look-ahead (MSLA) ASV optimal measurement location planning (OMLP) strategy is developed. This planning strategy prescribes future multi-step measurement locations. A physical interpretation of the proposed planner in the single-step, single transponder case is provided. Simulation results demonstrate the trade-off between expected localization performance and computational time associated with various look-ahead horizons and travel distances. Experimental results illustrate the proposed MSLA OMLP strategy's performance in environments containing one and two UTs. The proposed OMLP strategy is able to localize UTs to within 4 meters of their true locations. Additionally, increasing the planning horizon is demonstrated to yield better UT localization at the cost of increased computational burden.

Contents

List of Figures

List of Tables

Chapter 1

Introduction

Underwater vehicles require knowledge of their position to perform their mission [30]. Global navigation satellite system (GNSS) signals become severely attenuated underwater, rendering them unusable at depths below a few feet. Inertial navigation systems (INS) are prevalent in underwater navigation. To correct drifts inherent in INS, underwater vehicles may utilize a network of pre-deployed underwater transponders (UTs), surface vehicles, or resurfacing strategies [23], [16]. Resurfacing is not desirable in situations where stealth and covertness are required. This thesis focuses on localizing a set of UTs pre-deployed at unknown locations. Once the UT locations are known, they could serve as reference beacons for underwater navigation.

This thesis considers the following problem. An autonomous surface vehicle (ASV) makes acoustic range measurements to estimate the positions (i.e., localize) several pre-deployed UTs that are rigidly attached to the sea floor. Where should the ASV place itself to use range measurements to optimally localize the UTs?

This problem has similarities to optimal sensor placement, to which many optimization criteria have been developed [8, 22, 29, 39]. Among the most common optimization criteria is the D-optimality criterion, namely maximization of the logarithm of the determinant of the Fisher information matrix [36]. The D-optimality criterion yields the maximum reduction in target location uncertainty as measured by the volume of the uncertainty ellipsoid [28], [18]. An alternative criterion to D-optimality was proposed in [20], referred to as maximum innovative logarithm-determinant (MILD), which seeks to maximize the volume of the innovation matrix. MILD was shown to be both computationally efficient and identical to the D-optimality criterion under linear Gaussian assumptions and was demonstrated to yield comparable performance with nonlinear pseudorange measurements. Another computationally efficient criterion with a geometric interpretation that approximately minimizes the dilution of precision was proposed in [26]. This criterion was shown to yield a family of convex programs that can be solved in parallel. A collaborative sensor placement strategy was developed in [10], wherein a network of coordinated ASVs attempt to optimally place themselves to localize a single UT. The dual of this problem, wherein landmarks are optimally placed to aid in vehicle positioning, is explored in [31].

While classical sensor placement problems consider planar environments, a three-dimensional (3D) sensor placement strategy is needed for certain underwater and aerial applications. In underwater applications, an additional complexity arises from the fact that, once submerged, an autonomous underwater vehicle (AUV) is deprived of GNSS signals; hence, GNSS-derived positioning[1] information becomes unavailable. This forces a reliance

[1] In this thesis, the term 'positioning' refers to the vehicle estimating its own states. The term 'localization' will be used in reference to a vehicle estimating the states of some other entity.

on onboard inertial sensor suites that provide positioning estimates that deteriorate over time in the absence of an aiding source (e.g., GNSS or signals of opportunity [27]). Underwater simultaneous localization and mapping (SLAM) techniques have been developed to mitigate such deterioration [13].

Inertial sensors may be made robust to integral effects and drift via real-time corrections. This requires sensors (e.g., acoustic, magnetic, and pressure) to periodically correct for INS drift [25]. The standard long baseline (LBL) acoustic approach to aided inertial navigation uses an extended Kalman filter (EKF) to fuse ranges to multiple UTs with other AUV sensors [40]. An alternative approach to LBL was developed in [5], which uses an imaging sonar. Several magnetic/ geomagnetic field-aided approaches have been developed. The inversion of the gradient of the magnetic field vector associated with a magnetic dipole at a fixed, known location was proposed in [35]. Simulated results emphasize the improvement in navigation quality (i.e., the decrease in vehicle position error) by utilizing tensor Euler deconvolution in tandem with eigenanalysis of the magnetic gradient tensor. This work is motivated by the computational issues associated with analytical magnetic field inversion (i.e., when the magnetic field gradient tensor is singular). Another robust, computationally efficient algorithm for magnetic-aided navigation was developed in [7]. An adaptive unscented Kalman filter (UKF) for magnetic navigation in a SLAM framework (e.g., the magnetic dipole's position is unknown) was formulated in [37].

Environmental features may also be used to mitigate decay of quality of position estimates associated with inertial navigation. For example, a sonar-based terrain-aided navigation (TAN) framework was developed in [34] to aid an AUV. This is paired with

the work in [35] to develop a hybrid TAN-magnetic aided INS in [32]. This system was shown to yield lower AUV position error than either TAN or magnetic-aided navigation methods alone. An adaptive particle filter approach using sonar is developed in [41]. In [2], criteria were developed to ensure observability of the nonlinear system when ranging to a single acoustic beacon, while [19], [38] derive such criteria when measuring pseudoranges to multiple terrestrial signal transmitters.

Multi-step look-ahead (MSLA) planning, also known as model-predictive control (MPC) or receding horizon control, has seen several applications in SLAM-type problems. This scheme is adopted in [24] for AUV fleet formation control. In [15], MSLA trajectory planning was numerically evaluated for its prospective benefit in a robotic SLAM environment. A similar numerical evaluation was presented in [19] in both radio SLAM and mapping-only scenarios of several terrestrial transmitters using pseudorange measurements. A hybrid receding horizon path planner/model predictive AUV controller for dynamic navigation based on environmental information was developed in [33]. An adaptive path planning framework was developed in [6] to react to hazardous environments while maneuvering at high-speed. A receding horizon planner for anti-submarine warfare (ASW) AUV applications that is feasible in real-time was presented in [9]. The controller is able to drive the AUV in such a way as to minimize the localization error of a mobile undersea target based on measurements from a bistatic sonar array.

A single-step look-ahead OMLP strategy was developed in [11], which specifies the next optimal location at which the ASV should place itself to make acoustic range measurements to the UTs. This thesis makes three contributions. First, a maximum a

posteriori (MAP) framework is developed to localize UTs from noisy acoustic range measurements. Second, an MSLA optimal measurement location planning (OMLP) strategy is developed that plans future D-optimal measurement locations by specifying the ASV's yaw rate. Third, simulation and experimental results are presented demonstrating the superiority of the MSLA OMLP strategy over the single-step look-ahead as well as random ASV motion.

The refereed conference and journal publications resulting from this thesis are:

[C1] J. Garcia, J. Farrell, and Z. Kassas. Optimal measurement location planning for localizing underwater transponders. *In Proceedings of IEEE/ION Position Location and Navigation Symposium*, pages 480−486, April 2018.

[J1] J. Garcia, J. Farrell, Z. Kassas, and M. Ouimet. Autonomous surface vehicle measurement location planning for optimal underwater acoustic transponder localization. *IEEE Transactions on Aerospace and Electronic Systems*, 2018, submitted.

The remainder of this thesis is organized as follows. Chapter 2 describes the ASV's dynamics and observation model. Chapter 3 formulates the UT localization and MSLA OMLP problems for an arbitrary number of UTs in the environment. Chapter 4 presents a MAP approach to solve (1) the UT localization problem and (2) a computationally efficient approach to solve the OMLP problem. Chapter 5 presents simulation results demonstrating both solutions. Chapter 6 presents experimental results showing MSLA OMLP for one and two UTs with a localization accuracy of a few meters. Concluding remarks are given in Chapter 7.

Chapter 2

Model Description

The following nomenclature and conventions will be used throughout this thesis unless stated otherwise. Vectors will be column and represented by lower-case, italicized, and bold characters (e.g., $\boldsymbol{x}$). Matrices will be represented by upper-case bold characters (e.g., $\mathbf{X}$).

The symbol n will denote a specific measurement epoch, while N denotes the total number of measurements made by the ASV. The symbol M denotes the total number of UTs in the environment, while $m = 1, \cdots, M$ serves to index each UT. The symbol k corresponds to the number of steps planned by the MSLA OMLP. When $k = 0$, the ASV randomly plans the next measurement location.

2.1 Vehicle State and Model

Let $\boldsymbol{p}_V(n) \in \mathbb{R}^3$ represent the 3-D position of the ASV. The velocity of the ASV at measurement epoch n is $\boldsymbol{v}_V(n) \in \mathbb{R}^3$ and is represented in the vehicle's coordinate frame.

The optimal next location from which the ASV should make a measurement is $\boldsymbol{p}_V^*(n+1)$. This location is determined by solving an optimization problem that is constrained by a kinematic model with a maximum distance constraint.

To adopt an MSLA structure, the following model is assumed to propagate the ASV's position $\boldsymbol{p}_V$ and yaw angle ϕ_V:

$$\Sigma_V : \begin{cases} \boldsymbol{p}_V(n+1) & = \boldsymbol{p}_V(n) + \mathbf{R}_z\left[\phi_V(n+1)\right]\boldsymbol{v}_V(n)T \\ \phi_V(n+1) & = \phi_V(n) + \omega_V(n)T, \;\; n = 1, \cdots, N \end{cases}, \tag{2.1}$$

where T is the sampling period, ω_V is the yaw rate, and $\mathbf{R}_z$ is a rotation matrix about the z-axis of the local frame by angle ϕ_V, which has the form

$$\mathbf{R}_z\left[\phi_V(n)\right] = \begin{bmatrix} \cos(\phi_V(n)) & -\sin(\phi_V(n)) & 0 \\ \sin(\phi_V(n)) & \cos(\phi_V(n)) & 0 \\ 0 & 0 & 1 \end{bmatrix}. \tag{2.2}$$

The model in (2.1) assumes that T is sufficiently small such that ϕ_V and $\boldsymbol{v}_V$ over $nT \leq t < (n+1)T$ are constant.

The ASV's state is defined as $\boldsymbol{x}_V \triangleq \left[\boldsymbol{p}_V^\mathsf{T}, \phi_V\right]^\mathsf{T} \in \mathbb{R}^4$.

2.2 UT State and Model

It is assumed that M UTs exist in the environment at fixed, unknown positions. Let $\boldsymbol{p}_T^m \in \mathbb{R}^3$ be the position of the mth UT, which propagates according to $\boldsymbol{p}_T(n+1) = \boldsymbol{p}_T(n), n = 1, 2, \cdots, N$.

2.3 Observation Model

The acoustic range observation made by the ASV at the nth measurement epoch is related to the mth UT's position by

$$z^m(n) \;=\; r^m(n) + w(n), \tag{2.3}$$

where $r^m(n) \triangleq \|\boldsymbol{p}_V(n) - \boldsymbol{p}_T^m\|_2$ is the true range between the ASV and UT and $\|\cdot\|_2$ is the Euclidean norm, and w is the measurement noise, which is modeled as $w(n) \sim \mathcal{N}(0, \sigma^2)$ and assumed to be temporally independent as well as independent and identically distributed across all N measurement epochs. The vector of N range measurements to the mth UT is denoted by

$$\boldsymbol{z}^m = \boldsymbol{r}^m + \boldsymbol{w}^m \in \mathbb{R}^N, \tag{2.4}$$

where $\boldsymbol{r}^m \triangleq [r^m(1), \cdots, r^m(N)]^\mathsf{T}$ and $\boldsymbol{w}^m \triangleq [w^m(1), \cdots, w^m(N)]^\mathsf{T}$. The distribution of the measurement vector is $\boldsymbol{z}^m \sim \mathcal{N}(\boldsymbol{r}^m, \mathbf{R})$, where $\mathbf{R} = \sigma^2\, \mathbf{I}_{N\times N}$.

Chapter 3

UT Localization and MSLA OMLP Problem Formulation

This chapter formulates the UT localization and MSLA OMLP problems. The set of all ASV locations is denoted by ${}^{N}\mathcal{P}_V$. This set is constructed as

$$ {}^{N}\mathcal{P}_V \;=\; \{\boldsymbol{p}_V(1), \cdots, \boldsymbol{p}_V(N)\} \tag{3.1} $$

The ASV positions are assumed to be known (e.g., from GNSS measurements). The estimate of $\boldsymbol{p}_T^m$ based on N range measurements is denoted by $\hat{\boldsymbol{p}}_T^m(N)$. The range can be predicted as

$$ \hat{r}^m(n) \triangleq \|\hat{\boldsymbol{p}}_T^m(N) - \boldsymbol{p}_V(n)\|_2. \tag{3.2} $$

The vector of estimated ranges is

$$ \hat{\boldsymbol{r}}^m \triangleq [\hat{r}^m(1), \cdots, \hat{r}^m(N)]^{\mathsf{T}} \in \mathbb{R}^N. \tag{3.3} $$

The Jacobian vector $\boldsymbol{h}^m(n) \triangleq \left.\dfrac{\partial r^m(n)}{\partial \boldsymbol{p}_T^m}\right|_{\hat{\boldsymbol{p}}_T^m(n)}$ is

$$\boldsymbol{h}^m(n) = \frac{[\hat{\boldsymbol{p}}_T^m(N) - \boldsymbol{p}_V(n)]^\mathsf{T}}{\hat{r}^m(n)} \in \mathbb{R}^{1\times 3}. \tag{3.4}$$

The vectors in (3.4) can be stacked to form the matrix

$$\mathbf{H}^m = \left[(\boldsymbol{h}^m(1))^\mathsf{T}, \cdots, (\boldsymbol{h}^m(N))^\mathsf{T}\right]^\mathsf{T} \in \mathbb{R}^{N\times 3}. \tag{3.5}$$

Problem 1: UT Localization

Given all previous range measurements of the mth UT $\boldsymbol{z}^m$ made at ASV locations ${}^N\mathcal{P}_V$, estimate the position of the mth UT $\boldsymbol{p}_T^m$.

Problem 2: MSLA OMLP

Given the set of UT estimates using N range measurements $\{\hat{\boldsymbol{p}}_T^m(N)\}_{m=1}^M$, determine the next k values of the yaw rate $[\omega_V(N), \cdots, \omega_V(N+k-1)]$ that will drive the ASV to the locations $\{\boldsymbol{p}_V(N+1), \cdots, \boldsymbol{p}_V(N+k)\}$ in order to minimize the aggregate uncertainty of the set of future estimates $\{\hat{\boldsymbol{p}}_T^m(N+k)\}_{m=1}^M$, as measured by the logarithm of the determinant of the corresponding estimation error covariance.

Chapter 4

Solution to the UT Localization and MSLA OMLP Problems

This chapter presents solutions to the UT localization and OMLP problems, which were formulated in Chapter 3.

4.1 Solution to the UT Localization Problem

To reduce the linearization error on UT localization, an iterative Gauss-Newton approach is adopted [1] along with a MAP estimation formulation. The iterative estimation algorithm is initialized with an estimate and corresponding covariance, denoted by ${}_0\hat{\boldsymbol{p}}_T^m$ and ${}_0\mathbf{P}_T^m$, respectively, with the assumption ${}_0\hat{\boldsymbol{p}}_T^m \sim \mathcal{N}(\boldsymbol{p}_T^m, {}_0\mathbf{P}_T^m)$. In the case when one has little information about $\boldsymbol{p}_T^m$, ${}_0\mathbf{P}_T^m$ is set to be very large.

In what follows, the pre-subscript j denotes the iteration number. Specifically, the estimate of $\boldsymbol{p}_T^m$ at the jth iteration using N measurements is ${}_j\hat{\boldsymbol{p}}_T^m(N)$. Estimated ranges and

Jacobians at the jth iteration, ${}_j\hat{r}^m(n)$ and ${}_j\boldsymbol{h}^m(n)$, are computed by substituting ${}_j\hat{\boldsymbol{p}}_T^m(N)$ into (3.2) and (3.4). Similarly, ${}_j\hat{\boldsymbol{r}}^m$ and ${}_j\mathbf{H}^m$ are constructed by substituting ${}_j\hat{r}^m(n)$ and ${}_j\boldsymbol{h}^m(n)$, $\forall n \leq N$, into (3.3) and (3.5).

A MAP framework for UT localization is adopted [1, 21]. The basic optimization problem is

$$\hat{\boldsymbol{p}}_T^m(N) \triangleq \underset{\boldsymbol{p}_T^m}{\operatorname{argmax}} \left[p(\boldsymbol{z}^m \,|\, \boldsymbol{p}_T^m)\, p(\boldsymbol{p}_T^m) \right]. \tag{4.1}$$

Define the composite vectors

$$\boldsymbol{y} \;\triangleq\; \left[(\boldsymbol{z}^m)^\mathsf{T}, ({}_0\hat{\boldsymbol{p}}_T^m)^\mathsf{T} \right]^\mathsf{T} \tag{4.2}$$

$$\boldsymbol{f}(\boldsymbol{p}_T^m) \;\triangleq\; \left[(\boldsymbol{r}^m)^\mathsf{T}, (\boldsymbol{p}_T^m)^\mathsf{T} \right]^\mathsf{T}. \tag{4.3}$$

The covariance matrix for $\boldsymbol{y}$ is

$$\mathbf{C} \;=\; \text{blkdiag}\left[\mathbf{R}\,,\, ({}_0\mathbf{P}_T^m)\right]. \tag{4.4}$$

where blkdiag$(\cdot)$ denotes a block-diagonal matrix. Maximizing the objective function of (4.1) is equivalent to minimizing

$$\mathcal{J}_{MAP}(\boldsymbol{p}_T^m) \;\triangleq\; \frac{1}{2}\left[\boldsymbol{y} \,-\, \boldsymbol{f}(\boldsymbol{p}_T^m)\right]^\mathsf{T} \mathbf{C}^{-1} \left[\boldsymbol{y} \,-\, \boldsymbol{f}(\boldsymbol{p}_T^m)\right]. \tag{4.5}$$

This allows the maximization problem in (4.1) to be rewritten as

$$\hat{\boldsymbol{p}}_T^m(N) \triangleq \underset{\boldsymbol{p}_T^m}{\operatorname{argmin}} \quad \mathcal{J}_{MAP}(\boldsymbol{p}_T^m). \tag{4.6}$$

The MAP estimate of $\boldsymbol{p}_T^m$ is computed by solving the batch nonlinear least-squares optimization problem in (4.6) iteratively according to the following steps. Start the iteration counter with $j = 0$. Let the jth estimate of $\boldsymbol{p}_T^m$ be ${}_j\hat{\boldsymbol{p}}_T^m$. The estimated range vector is

${}_j\hat{\boldsymbol{r}}^m = \boldsymbol{r}^m|_{\boldsymbol{p}_T^m = {}_j\hat{\boldsymbol{p}}_T^m}$. The vector $\boldsymbol{f}(\boldsymbol{p}_T^m)$ is linearized around ${}_j\hat{\boldsymbol{p}}_T^m$ at each iteration, yielding

$$\boldsymbol{f}(\boldsymbol{p}_T^m) \approx \boldsymbol{f}({}_j\hat{\boldsymbol{p}}_T^m) + \mathbf{V}_j\,\delta\boldsymbol{p}_j, \tag{4.7}$$

where

$$\mathbf{V}_j \triangleq \begin{bmatrix} \mathbf{H}^m({}_j\hat{\boldsymbol{p}}_T^m) \\ \mathbf{I}_{3\times 3} \end{bmatrix} \in \mathbb{R}^{(N+3)\times 3} \tag{4.8}$$

$$\delta\boldsymbol{p}_j \triangleq \boldsymbol{p}_T^m - {}_j\hat{\boldsymbol{p}}_T^m. \tag{4.9}$$

Define $\delta\boldsymbol{y}_j \triangleq \boldsymbol{y} - \boldsymbol{f}({}_j\hat{\boldsymbol{p}}_T^m)$ to simplify notation. The MAP objective function in (4.6) can be re-expressed as

$$\mathcal{J}_{MAP}(\delta\boldsymbol{p}_j) = (\delta\boldsymbol{y}_j - \mathbf{V}_j\,\delta\boldsymbol{p}_j)^{\mathsf{T}}\mathbf{C}^{-1}(\delta\boldsymbol{y}_j - \mathbf{V}_j\,\delta\boldsymbol{p}_j). \tag{4.10}$$

The linearized objective function (4.10) is minimized when

$$\delta\boldsymbol{p}_j \equiv (\mathbf{V}_j^{\mathsf{T}}\mathbf{C}^{-1}\mathbf{V}_j)^{-1}\mathbf{V}_j^{\mathsf{T}}\mathbf{C}^{-1}\delta\boldsymbol{y}_j. \tag{4.11}$$

The estimate at the next iteration is

$${}_{j+1}\hat{\boldsymbol{p}}_T^m = {}_j\hat{\boldsymbol{p}}_T^m + \delta\boldsymbol{p}_j. \tag{4.12}$$

The iterations continue until $\|{}_{j+1}\hat{\boldsymbol{p}}_T^m - {}_j\hat{\boldsymbol{p}}_T^m\|_2 \leq \delta_{min}$, or as long as $j \leq J_{max}$, for user-defined J_{max} and δ_{min}. After convergence, the covariance is

$${}^N\mathbf{P}_T^m \equiv (\mathbf{V}_j^{\mathsf{T}}\mathbf{C}^{-1}\mathbf{V}_j)^{-1}. \tag{4.13}$$

4.2 Solution to the MSLA OMLP Problem

The D-optimality criterion [4, p. 387] is used to determine the future k-step trajectory $\{\boldsymbol{p}_V(N+n)\}_{n=1}^k$ to maximize the information gain. For this section, the subscript

N corresponds to the number of previous ASV locations. The symbol $\mathbf{Y}_N^m \in \mathbb{R}^{3\times 3}$ denotes the information matrix after N ASV measurements to the mth UT (i.e., $\mathbf{Y}_N^m = ({}^N\mathbf{P}_T^m)^{-1}$).

The single-step look-ahead (i.e., $k = 1$), commonly referred to as a greedy strategy, was formulated in [11] as

$$\begin{aligned} \boldsymbol{x}^* &= \underset{\boldsymbol{x}}{\operatorname{argmax}} \quad \mathcal{J}(\boldsymbol{x}) \\ &\quad \text{subject to} \quad g(\boldsymbol{x}) \leq d_{max}, \end{aligned} \tag{4.14}$$

where

$$\mathcal{J}(\boldsymbol{x}) \triangleq \log\det\left[\mathbf{Y}_{N+1}(\boldsymbol{x})\right] \tag{4.15}$$

$$\mathbf{Y}_{N+1} \triangleq \operatorname{diag}\left[\mathbf{Y}_{N+1}^1, \cdots, \mathbf{Y}_{N+1}^M\right] \tag{4.16}$$

$$g(\boldsymbol{x}) \triangleq \|\boldsymbol{x} - \boldsymbol{p}_V(N)\|_2 \tag{4.17}$$

$$\boldsymbol{x} \triangleq \boldsymbol{p}_V(N+1). \tag{4.18}$$

The distance constraint d_{max} represents the maximum distance the ASV may travel between epochs N and $N+1$.

The single-step OMLP was generalized to the MSLA OMLP in [12]. Define

$$\mathbf{D}_{N+k}^m(\omega_k) \triangleq \left(\boldsymbol{h}^m(N+k)\right)^\mathsf{T} \boldsymbol{h}^m(N+k),$$

where the symbol $\omega_k \triangleq \omega_V(N+k-1)$ is used to simplify notation. Recall from (3.3) that $\boldsymbol{h}^m(N+k)$ depends on ω_k because $\omega_V(\cdot)$ is integrated through (2.1) to determine ${}^{N+k}\mathcal{P}_V$.

The information about transponder m at epoch $N+k$ may be expressed as

$$\begin{aligned} \mathbf{Y}_{N+k}^m(\omega_k) &\triangleq \sigma^{-2}\left(\mathbf{H}_{N+k}^m\right)^\mathsf{T}\mathbf{H}_{N+k}^m \\ &= \sigma^{-2}\left[\left(\mathbf{H}_{N+k-1}^m\right)^\mathsf{T}\mathbf{H}_{N+k-1}^m + \mathbf{D}_{N+k}^m(\omega_k)\right] \\ &= \mathbf{Y}_{N+k-1}^m + \sigma^{-2}\mathbf{D}_{N+k}^m(\omega_k). \end{aligned} \tag{4.19}$$

The information $\mathbf{Y}_{N+k}^{m}$ may be expressed as a function of $\mathbf{Y}_{N}^{m}$ by recursively using (4.19)

$$\mathbf{Y}_{N+k}^{m}(\boldsymbol{\omega}_V) \;=\; \mathbf{Y}_{N}^{m} + \sigma^{-2}\sum_{n=1}^{k}\mathbf{D}_{N+n}^{m}\left(\omega_n\right), \tag{4.20}$$

where $\boldsymbol{\omega}_V = \{\omega_n\}_{n=1}^{k}$.

The MSLA D-optimality problem is

$$\begin{aligned} \boldsymbol{\omega}_{\boldsymbol{V}}^{*} \;&= \underset{\boldsymbol{\omega}_{\boldsymbol{V}}}{\operatorname{argmax}} \qquad \mathcal{J}(\boldsymbol{\omega}_{\boldsymbol{V}}) \\ &\quad \text{subject to} \quad \Sigma_V \\ &\qquad\qquad\qquad \{g(\boldsymbol{\omega}_V(n)) \leq \;\omega_{max}\}_{n=1}^{k}, \end{aligned} \tag{4.21}$$

where

$$\mathcal{J}(\boldsymbol{\omega}_V) \;\triangleq\; \log\det\left[\mathbf{Y}_{N+k}\left(\boldsymbol{\omega}_V\right)\right] \tag{4.22}$$

$$\mathbf{Y}_{N+k} \;\triangleq\; \operatorname{diag}\left[\mathbf{Y}_{N+k}^{1}, \cdots, \mathbf{Y}_{N+k}^{M}\right] \tag{4.23}$$

$$g(\boldsymbol{\omega}_V(n)) \;\triangleq\; |\omega_n|. \tag{4.24}$$

The distance constraint in (4.14) is subsumed into $\boldsymbol{v}_V$ in (2.1). The angular rate constraint $g(\boldsymbol{\omega}_V(n))$ restricts each ω_n to an envelope of $\pm\,\omega_{max}$. Notice that $\mathbf{Y}_{N+k}^{m}(\boldsymbol{\omega}_V)$ is determined via linearization about estimate $\hat{\boldsymbol{p}}_T^{m}(N)$. The first element of $\boldsymbol{\omega}_V^{*}$, namely ω_1^{*}, is applied to maneuver the ASV to obtain $\boldsymbol{x}_V(N+1)$ (cf. (2.1)), while the remaining elements $\omega_2^{*}, \cdots, \omega_k^{*}$ are discarded. Note that these elements are discarded since at the next epoch, the ASV will receive new acoustic measurements which will be used to obtain a "refined" solution by solving the MSLA again (i.e., recede the planning horizon). Also note that while these elements are discarded, they impact the obtained optimal solution ω_1^{*}, which is computed as part of the multi-step vector $\boldsymbol{\omega}_V^{*}$.

Next, the MSLA D-optimality problem (4.21) is simplified by exploiting the block diagonal structure of $\mathbf{Y}_{N+k}(\boldsymbol{\omega}_V)$ to write

$$\begin{aligned} \boldsymbol{\omega}_V^* &= \underset{\boldsymbol{\omega}_V}{\operatorname{argmax}} \qquad \log f(\boldsymbol{\omega}_V) \\ &\qquad \text{subject to} \quad \Sigma_V \\ &\qquad\qquad \{g(\boldsymbol{\omega}_V(n)) \leq \ \omega_{max}\}_{n=1}^{k}, \end{aligned} \tag{4.25}$$

where $f(\boldsymbol{\omega}_V) = \prod_{m=1}^{M} \det\left[\mathbf{Y}_{N+k}^m(\boldsymbol{\omega}_V)\right]$. Using the properties of the logarithm function,

$$\log f(\boldsymbol{\omega}_V) = \sum_{m=1}^{M} \log\det\left[\mathbf{Y}_{N+k}^m(\boldsymbol{\omega}_V)\right]. \tag{4.26}$$

Further simplifications may be made if $\sigma^{-2}\sum_{n=1}^{k}\mathbf{D}_{N+n}^m(x_n)$ is linearly seperable, i.e., if

$$\mathbf{Y}_{N+k}^m(\boldsymbol{\omega}_V) \ = \ \mathbf{Y}_N^m + \boldsymbol{d}_1(\boldsymbol{\omega}_V)\boldsymbol{d}_2^{\mathsf{T}}(\boldsymbol{\omega}_V),$$

where the vectors $\boldsymbol{d}_i(\boldsymbol{\omega}_V) \in \mathbb{R}^{3\times 1}$, $i = 1, 2$. While this decomposition may not hold in general, it is clear from the form of (4.20) that this is true when $k = 1$. In this case, $\boldsymbol{d}_i(\boldsymbol{\omega}_V) = (\boldsymbol{h}^m(N{+}1))^{\mathsf{T}}$. When this decomposition holds, the matrix determinant properties developed in Appendix A, namely (A.7), could be applied to (4.26) to give

$$\det\left[\mathbf{Y}_{N+k}^m(\boldsymbol{\omega}_V)\right] \ = \ \det[\mathbf{Y}_N^m]\cdot\det[1 + \boldsymbol{d}_2^{\mathsf{T}}(\boldsymbol{\omega}_V)(\mathbf{Y}_N^m)^{-1}\,\boldsymbol{d}_1(\boldsymbol{\omega}_V)]. \tag{4.27}$$

Define

$$\alpha^m(\boldsymbol{\omega}_V) \ \triangleq \ \boldsymbol{d}_2^{\mathsf{T}}(\boldsymbol{\omega}_V)(\mathbf{Y}_N^m)^{-1}\,\boldsymbol{d}_1(\boldsymbol{\omega}_V), \tag{4.28}$$

which is a positive scalar. Using (4.27)-(4.28), the optimization function in (4.26) can be simplified to

$$\log f(\boldsymbol{\omega}_V) = \sum_{m=1}^{M} \log\Big[\,[1 + \alpha^m(\boldsymbol{\omega}_V)]\det[\mathbf{Y}_N^m]\Big]. \tag{4.29}$$

Properties of the logarithm function allow further simplification to

$$\log f(\boldsymbol{\omega}_V) = \sum_{m=1}^{M} \log\left[1 + \alpha^m(\boldsymbol{\omega}_V)\right] + \sum_{m=1}^{M} \log\det[\mathbf{Y}_N^m]. \tag{4.30}$$

The term $\sum_{m=1}^{M} \log\det[\mathbf{Y}_N^m]$ is constant with respect to $\boldsymbol{\omega}_V$, so it can be dropped from the optimization function.

Letting $\bar{\mathcal{J}}(\boldsymbol{\omega}_V) \triangleq \sum_{m=1}^{M} \log\left[1 + \alpha^m(\boldsymbol{\omega}_V)\right]$, the optimization problem of (4.25) can be written as

$$\begin{aligned} \boldsymbol{\omega}_V^* &= \underset{\boldsymbol{\omega}_V}{\operatorname{argmax}} \quad \bar{\mathcal{J}}(\boldsymbol{\omega}_V) \\ &\quad \text{subject to} \quad \Sigma_V \\ &\qquad \{g(\boldsymbol{\omega}_V(n)) \leq \omega_{max}\}_{n=1}^{k}. \end{aligned} \tag{4.31}$$

Note that for $M = 1$, (4.26) is the same as

$$\begin{aligned} \boldsymbol{\omega}_V^* &= \underset{\boldsymbol{\omega}_V}{\operatorname{argmax}} \quad \bar{\mathcal{J}}'(\boldsymbol{\omega}_V) \\ &\quad \text{subject to} \quad \Sigma_V \\ &\qquad \{g(\boldsymbol{\omega}_V(n)) \leq \omega_{max}\}_{n=1}^{k}, \end{aligned} \tag{4.32}$$

where $\bar{\mathcal{J}}'(\boldsymbol{\omega}_V) \triangleq \alpha(\boldsymbol{\omega}_V)$.

Chapter 5

Simulation Results

This chapter presents simulation results for the UT localization and MSLA OMLP problems. The following quantitative metrics will be used in this chapter. Define the position error vector of the mth UT at the nth epoch as

$$\tilde{\boldsymbol{p}}_T^m(n) \triangleq \boldsymbol{p}_T^m - \hat{\boldsymbol{p}}_T^m(n) \in \mathbb{R}^3. \tag{5.1}$$

The augmented position error vector for all M UTs is

$$\tilde{\boldsymbol{p}}_T(n) \triangleq \left[\left(\tilde{\boldsymbol{p}}_T^1(n)\right)^{\mathsf{T}}, \cdots, \left(\tilde{\boldsymbol{p}}_T^M(n)\right)^{\mathsf{T}}\right]^{\mathsf{T}} \in \mathbb{R}^{3M}. \tag{5.2}$$

The magnitude of the position error vector is $\|\tilde{\boldsymbol{p}}_T^m(n)\|_2$. The normalized estimation error squared (NEES) at epoch n is

$$\epsilon(n) \triangleq \tilde{\boldsymbol{p}}_T^{\mathsf{T}}(n)\mathbf{Y}_n\tilde{\boldsymbol{p}}_T(n). \tag{5.3}$$

The localization performance is evaluated using Monte Carlo tests. Let $c \in \{1, 2, \cdots, C\}$ be the index of a specific Monte Carlo trial. The localization root-mean-square estimation

error (RMSEE) of the mth UT at the nth epoch is defined as

$$\bar{p}_T^m(n) \triangleq \sqrt{\frac{1}{C}\sum_{c=1}^{C}\|\tilde{\boldsymbol{p}}_T^m(n)\|_2^2}. \tag{5.4}$$

The D-optimal value at the nth measurement epoch is denoted by $\log\det[\mathbf{Y}_n]$. The average computational time will be denoted by $\bar{t}_c$.

5.1 Gauss-Newton MAP estimator for UT localization

The Gauss-Newton MAP estimator developed in Chapter 4.1 assumes the measurement noise to be independent across different UT range measurements. Therefore, each UT may be estimated independently. This section evaluates the Gauss-Newton MAP estimator on a single UT for a pre-described ASV trajectory. The superscript $m = 1$ is dropped in this section. A Monte Carlo analysis is performed, simulating 500 runs of the MAP estimation algorithm. For each run, the ASV made $N = 4$ measurements from the locations listed in Table 5.1 to localize $\boldsymbol{p}_T$.

Table 5.1: ASV locations used in Monte Carlo analysis

Symbol	$\boldsymbol{p}_V(1)$	$\boldsymbol{p}_V(2)$	$\boldsymbol{p}_V(3)$	$\boldsymbol{p}_V(4)$
Value, m	$\begin{bmatrix}5\\5\\0\end{bmatrix}$	$\begin{bmatrix}-5\\5\\0\end{bmatrix}$	$\begin{bmatrix}-5\\-5\\0\end{bmatrix}$	$\begin{bmatrix}5\\-5\\0\end{bmatrix}$

The UT was fixed at $\boldsymbol{p}_T = [17, 15, -6]^\mathsf{T}$. The value ${}_0\hat{\boldsymbol{p}}_T$ was drawn from a Gaussian distribution with covariance ${}_0\mathbf{P}_T = \text{diag}[100, 100, 4]$ and mean $\boldsymbol{p}_T$. The USBL measurement

noise, defined in (2.4), has $\sigma = 0.1$ m based on the SeaTrac x150 USBL product sheet [3].

The actual 95% confidence ellipse was calculated in the Easting-Northing (E-N) plane by substituting the upper-left 2×2 block of (4.13) and associated elements of (4.12) into the equations of Appendix B. Also, the estimated 95% confidence ellipse fitted to 500 samples of $\hat{\boldsymbol{p}}_T(4)$ was calculated in the E-N plane using the equations in Appendix B. Fig. 5.1 compares these ellipses and shows them to be comparable.

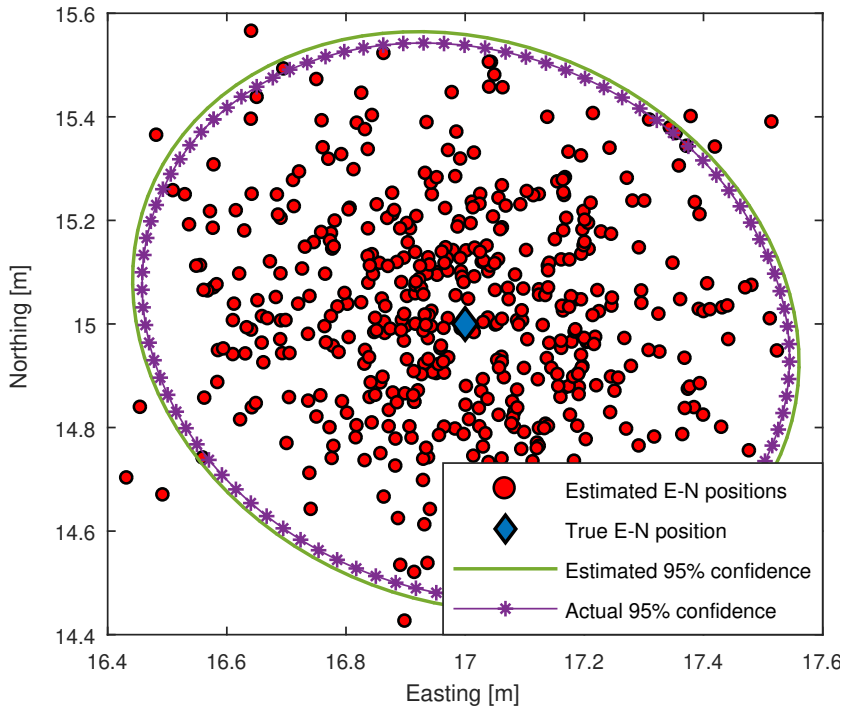

Figure 5.1: Scatter plot of $\hat{\boldsymbol{p}}_T(4)$ in the $E - N$ plane.

The NEES of the MAP estimator will be evaluated next. It is expected that $\epsilon(n) \sim \chi^2_{3M}$ (i.e., has a chi-squared probability density function (pdf) with $3M$ degrees-of-freedom). Fig. 5.2 displays a normalized histogram of (5.3) at epoch $n = N = 4$ across all Monte Carlo runs. A curve corresponding to a χ^2_3 distribution is overlayed onto this

histogram. The curve fits the values of (5.3) closely, further validating that the estimator is performing correctly.

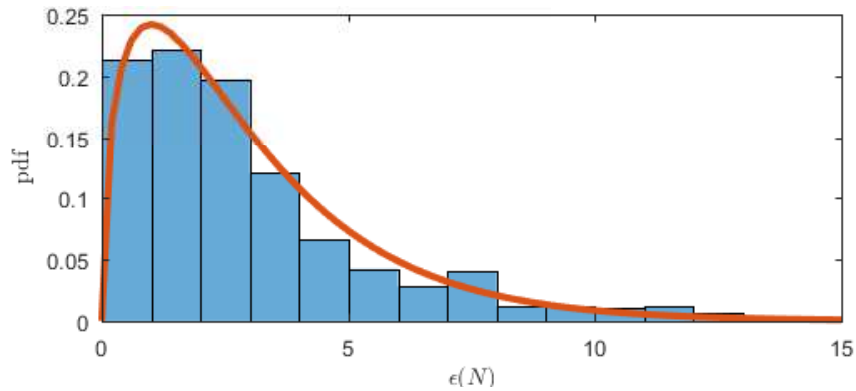

Figure 5.2: Histogram of (5.3) at measurement epoch $n = N = 4$ for all Monte Carlo runs. The orange curve displays a χ^2_3 pdf.

5.2 OMLP Evaluation for M = 1

This section evaluates the OMLP strategy for the single UT environment (the superscript m is dropped from this section). A Monte Carlo analysis is performed, consisting of 500 runs of 50 (i.e., $N = 50$) simulated acoustic measurements. Table 5.2 summarizes the simulation settings. The initial UT location ${}_0\hat{\boldsymbol{p}}_T$ is drawn from a Gaussian distribution with mean $\boldsymbol{p}_T$ and covariance ${}_0\mathbf{P}_T = \text{diag}[10^4, 10^4, 4]$ for all Monte Carlo runs. The OMLP results are compared to those obtained from a random ASV trajectory, subject to the same maximum distance constraint outlined in (4.14) to demonstrate the benefit gained from planing measurement locations (in a greedy sense) to improve UT localization.

It is expected that the D-optimal value obtained by following the OMLP strategy will be larger than that obtained by random ASV motion. This in turn should yield

Table 5.2: OMLP Single UT Localization Simulation Settings

Symbol	$\boldsymbol{p}_V(1)$	$\boldsymbol{p}_T$	T	d_{max}	σ
Value	$\begin{bmatrix} -3 \\ 9 \\ 0 \end{bmatrix}$ m	$\begin{bmatrix} 17 \\ 15 \\ -6 \end{bmatrix}$ m	1 s	5 m	0.12 m

smaller values of RMSEE. The data provided in Table 5.3 confirms these expectations, demonstrating the benefit of planning measurement locations.

Table 5.3: OMLP Single UT Localization Simulation Results

epoch	k	$\bar{p}_T(n)$[m]	$\log\det[\mathbf{Y}_n]$	$\sigma_{\log\det[\mathbf{Y}_n]}$
$n = 3$	0	4.21	3.61	1.18
	1	1.87	4.56	0.09
$n = 7$	0	1.79	6.86	0.64
	1	1.51	8.95	0.28
$n = 30$	0	0.94	11.25	0.57
	1	0.09	18.63	0.08

It is worth noting that the solution to the unconstrained maximization of (4.28) is achieved when $\boldsymbol{h}^m(N+1)$ lies along the eigenvector associated with the largest eigenvalue of $\mathbf{Y}_N$. This in turn yields a $\boldsymbol{p}_V(N+1)$ along this eigenvector when d_{max} is sufficiently large. Fig. 5.3[1] displays the resulting $\boldsymbol{p}_V^*(2)$ determined from a subset of $d_{max} \in [1, 80]$ m. Note that $\boldsymbol{p}_V^*(2)$ always lies at the point along the boundary of the feasible region that minimizes

[1]Two optimal measuring locations $\boldsymbol{p}_V^*(N+1)$ exist. Fig. 5.3 focuses on those solutions that lie along the axis pointing northwest

$||\boldsymbol{p}_V^*(2) - \boldsymbol{v}_{max}||_2$, where $\boldsymbol{v}_{max}$ is the eigenvector corresponding to the largest eigenvalue of $\mathbf{Y}_1$.

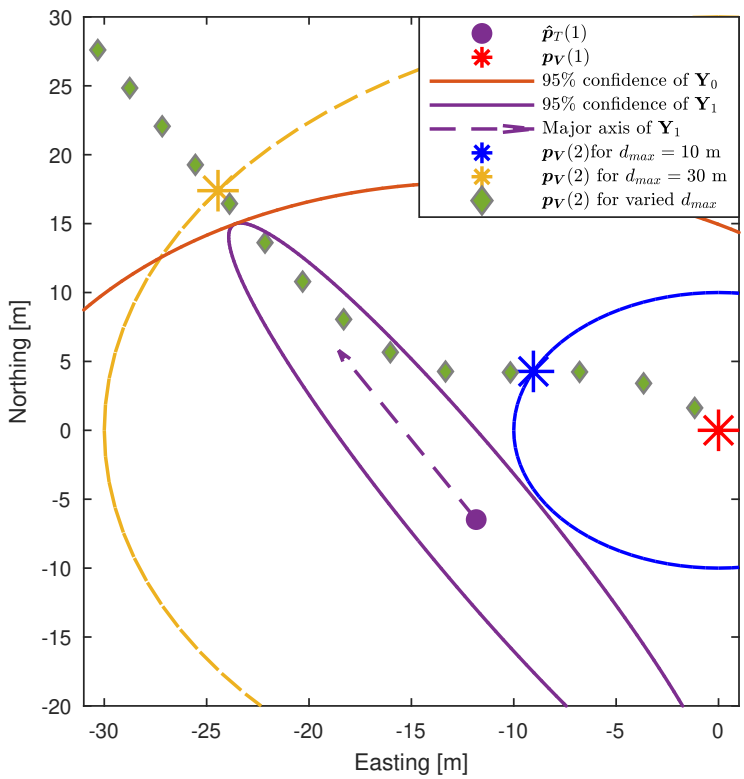

Figure 5.3: Optimally planned ASV measurement locations determined at epoch $n = 1$. The green sequence of diamonds indicates the optimal solution $\boldsymbol{p}_V^*(2)$ as a function of v_x. The red asterisk denotes $\boldsymbol{p}_V(1)$. The eigenvector corresponding to the largest eigenvalue of $\mathbf{Y}_1$ is denoted by the dashed purple arrow pointing in the direction of the major axis of the purple ellipse.

5.3 MSLA OMLP Evaluation for M = 1

This section evaluates the MSLA OMLP for the single UT environment (the superscript m is dropped from this section). Again, a Monte Carlo analysis is performed. For this analysis, 1000 runs consisting of 50 (i.e., $N = 50$) acoustic measurements were simu-

lated. Table 5.4 summarizes the simulation settings. The initial UT location ${}_0\hat{\boldsymbol{p}}_T$ is drawn from a Gaussian distribution with mean $\boldsymbol{p}_T$ and covariance ${}_0\mathbf{P}_T = \text{diag}[10^4, 10^4, 4]$ for all Monte Carlo runs. Three look-ahead lengths were simulated: $k = 1$, 2, and 3. Additionally, a random ASV trajectory ($k = 0$) was simulated, subject to the constraints in (4.25) to demonstrate the benefit gained from planning the measurement locations to improve UT localization.

Table 5.4: MSLA OMLP Single UT Localization Simulation Settings

Symbol	$\boldsymbol{p}_V(1)$	$\phi_V(1)$	$\boldsymbol{p}_T$	T	$\boldsymbol{v}_V$	ω_{max}	σ
Value	$\begin{bmatrix} -3 \\ 9 \\ 0 \end{bmatrix}$ m	-30°	$\begin{bmatrix} 17 \\ 15 \\ -6 \end{bmatrix}$ m	1 s	$\begin{bmatrix} 3 \\ 0 \\ 0 \end{bmatrix}$ m/s	30 °/s	0.12 m

It is expected that the D-optimal value obtained by using larger values of k will be larger than those obtained for smaller k at the cost of longer average computational time. However, due to the linearizations made in (4.20), there may be discrepancies in this trend at earlier measurement epochs. This trend in D-optimal value should in turn yield smaller values of (5.4). Additionally, it is intuitive to expect (5.4) and the D-optimal value to approach lower and upper bounds, respectively, determined by the number of measurements N, limiting the performance enhancements achievable by increasing k.

Fig. 5.4 displays the D-optimal value and (5.4) for various values of k as functions of n. These values are averaged over all Monte Carlo runs. Table 5.5 presents results for this simulation at specific epochs indicated by n. Rows of this table organize data for different

look-ahead duration indicated by k.

It is clear from Table 5.5 that the expected data trend holds in general. However, there are discrepancies in certain values at certain epochs. Nevertheless, these discrepancies are insignificant considering the magnitude of the standard deviation associated with these values at these epochs (the last column of Table 5.5). The value $\bar{t}_c$ (in seconds) increases from 0.18 s when $k = 1$, to 0.43 s when $k = 2$, to 0.88 s when $k = 3$.

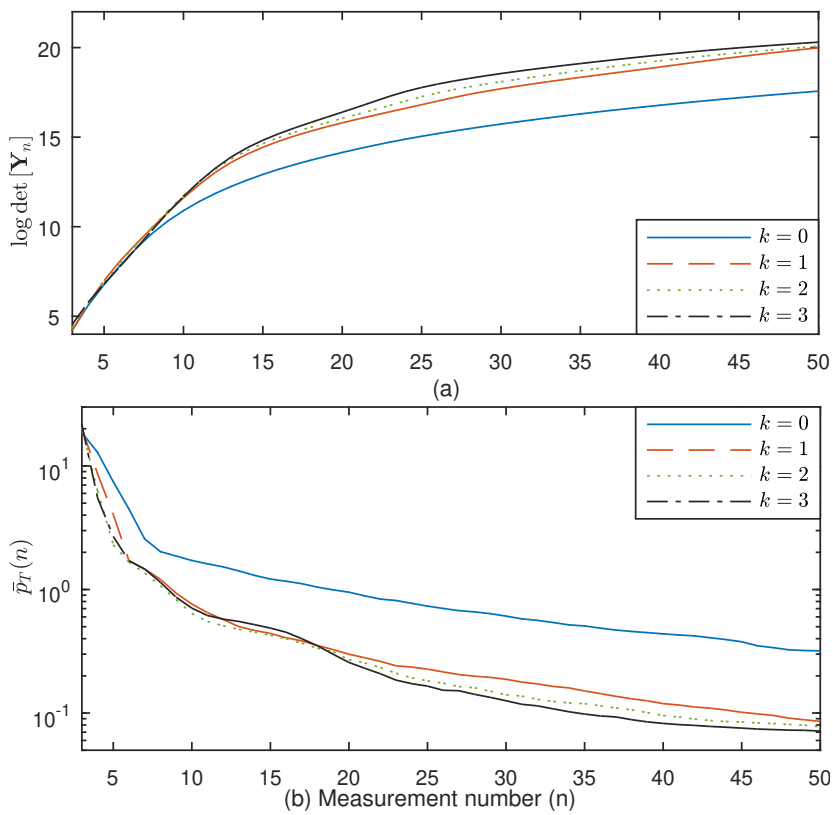

Figure 5.4: Evolution of (a) D-optimal value and (b) localization RMSEE (5.4) as functions of measurement number n. These values are shown for various values of k ($k = 0$ denotes a random ASV trajectory).

It is worthwhile to verify the consistency of the estimator developed in Chapter

Table 5.5: MSLA OMLP Single UT Localization Simulation Results

epoch	k	$\bar{p}_T(n)$[m]	$\log\det[\mathbf{Y}_n]$	$\sigma_{\log\det[\mathbf{Y}_n]}$
$n = 3$	0	18.61	4.24	0.70
	1	20.06	4.22	0.94
	2	20.37	4.38	0.80
	3	21.55	4.55	0.51
$n = 7$	0	2.56	8.77	0.65
	1	1.46	9.02	0.87
	2	1.36	8.98	0.93
	3	1.46	8.77	0.84
$n = 30$	0	0.61	15.73	1.68
	1	0.19	17.70	1.34
	2	0.14	18.10	1.13
	3	0.13	18.55	0.95

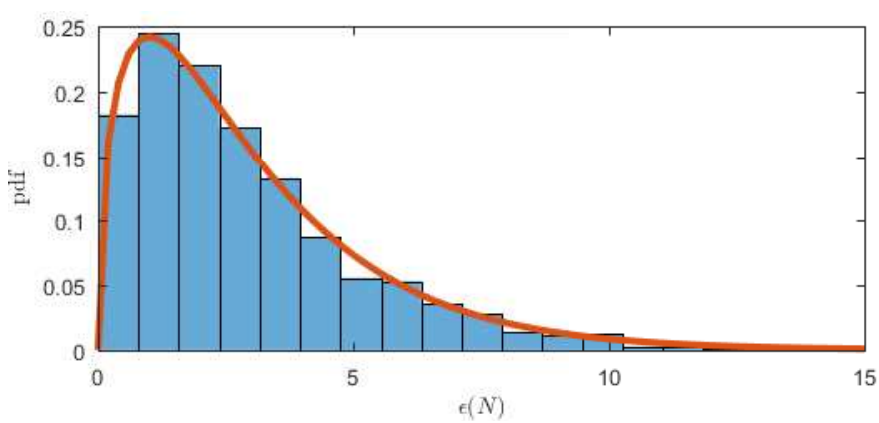

Figure 5.5: Histogram of (5.3) at measurement epoch $n = N = 50$ for all Monte Carlo runs in a single UT setup. The orange curve displays a χ^2_3 pdf.

4.1 when applied to the MSLA OMLP problem. The normalized position error (5.3) may be examined as in Chapter 5.1. It is expected that (5.3) will be distributed according to a chi-squared pdf with $3M = 3$ degrees of freedom. Fig. 5.5 presents the histogram of this value at measurement epoch $n = N$ over all Monte Carlo runs for the $k = 2$ planner. It is clear that (5.3) follows the expected distribution, suggesting the estimator is consistent. This trend was observed for the values of $k = 1$ and $k = 3$ as well.

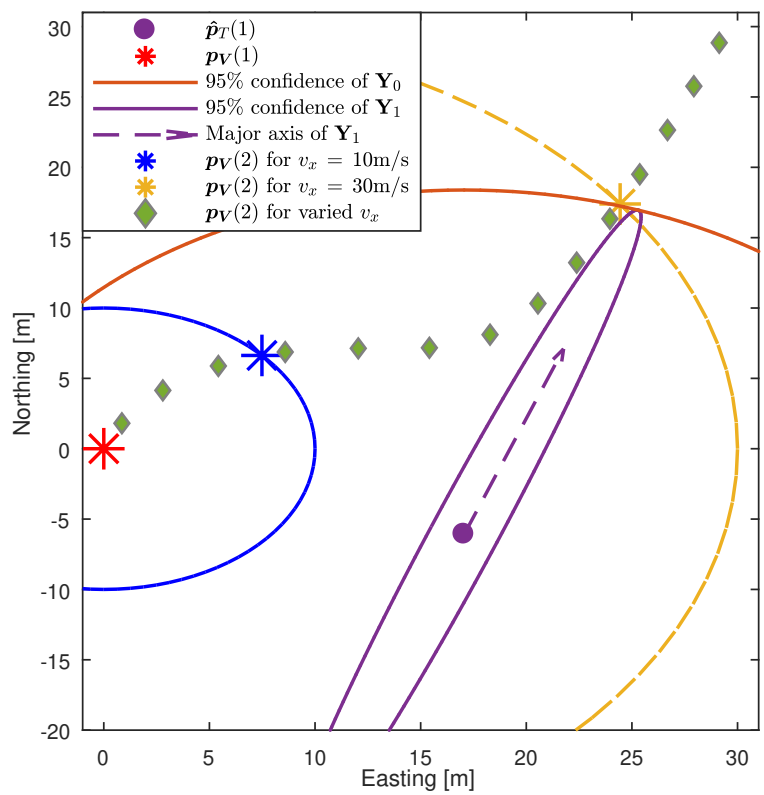

Figure 5.6: Optimally planned ASV measurement locations determined at epoch $n = 1$ for $k = 1$. The green sequence of diamonds indicates the optimal solution $\boldsymbol{p}_V^*(2)$ as a function of v_x. The red asterisk denotes $\boldsymbol{p}_V(1)$. The eigenvector corresponding to the largest eigenvalue of $\mathbf{Y}_1$ is denoted by the dashed purple arrow pointing in the direction of the major axis of the purple ellipse.

It was demonstrated in Chapter 5.2 that the solution to the greedy OMLP problem

is achieved when $\boldsymbol{h}(N+1)$ is collinear with the eigenvector associated with the largest eigenvalue of $\mathbf{Y}_N$. This solution could be achieved by increasing the maximum allowable distance the ASV could move between measurements. In the MSLA OMLP framework, however, this solution requires varying the ASV's forward velocity, denoted by v_x, while fixing $\omega_{max} = \frac{180°}{T}$. This demonstration focuses on the planned ASV location after the first measurement has been made (i.e., $N = 1$). Fig. 5.6[2] displays the resulting $\boldsymbol{p}_V^*(2)$ as v_x is varied from 1 m/s to 80 m/s in increments of 1 m/s. To avoid clutter, this figure displays $\boldsymbol{p}_V^*(2)$ determined using a subset of $v_x \in [1, 80]$ m/s. It is clear that this result is consistent with that presented in Chapter 5.2.

5.4 OMLP Evaluation for M = 4

This section evaluates the OMLP approach in a multi-UT environment. Again, a Monte Carlo analysis is performed consisting of 500 runs of 50 simulated acoustic range measurements. Constants for this analysis are collected in Table 5.6. As in Chapter 5.2, the initial UT location ${}_0\hat{\boldsymbol{p}}_T$ is drawn from a Gaussian distribution with mean $\boldsymbol{p}_T$ and covariance ${}_0\mathbf{P}_T = \text{diag}[10^4, 10^4, 4]$ for all Monte Carlo runs. As in Chapter 5.2, the OMLP ASV trajectory was compared to a random ASV trajectory to demonstrate the localization benefits gained when planning measurement locations.

Results of this simulation are presented in Table 5.7. This table presents the D-optimal value and RMSEE averaged over all Monte Carlo runs for both the OMLP and random trajectories at specific measurement epochs. Again, it can be seen that planning

[2]Two optimal measuring locations $\boldsymbol{p}_V^*(N+1)$ exist. Fig. 5.6 focuses on those solutions that lie along the axis pointing northeast.

Table 5.6: OMLP Multiple UT ($M = 4$) Localization Simulation Settings

Symbol	$\boldsymbol{p}_V(1)$	$\boldsymbol{p}_T^1$	$\boldsymbol{p}_T^2$	$\boldsymbol{p}_T^3$	$\boldsymbol{p}_T^4$	T	d_{max}	σ
Value	$\begin{bmatrix} -3 \\ 9 \\ 0 \end{bmatrix}$ m	$\begin{bmatrix} 17 \\ 15 \\ -6 \end{bmatrix}$ m	$\begin{bmatrix} -2 \\ -1 \\ -7 \end{bmatrix}$ m	$\begin{bmatrix} 5 \\ 5 \\ -10 \end{bmatrix}$ m	$\begin{bmatrix} -9 \\ 13 \\ -8 \end{bmatrix}$ m	1 s	5 m	0.12 m

measurement locations significantly improves localization results, namely D-optimal value.

Table 5.7: OMLP Multiple UT ($M = 4$) Localization Simulation Results

epoch	k	$\bar{p}_T^{m=2}(n)$[m]	$\log\det[\mathbf{Y}_n]$	$\sigma_{\log\det[\mathbf{Y}_n]}$
$n = 3$	0	1.50	24.03	3.99
	1	0.66	29.94	0.97
$n = 7$	0	1.21	39.15	2.45
	1	0.35	48.71	1.71
$n = 30$	0	0.59	54.51	2.12
	1	0.08	76.61	0.44

5.5 MSLA OMLP Evaluation for M = 4

This section evaluates the MSLA OMLP for a multi-UT environment with $M = 4$. A Monte Carlo analysis with 1000 runs is performed in an identical fashion to that in Chapter 5.3 with the simulation settings tabulated in Table 5.8.

Fig. 5.7 displays the D-optimal value and (5.4) for various values of k as functions

Table 5.8: MSLA OMLP Multiple UT ($M = 4$) Localization Simulation Settings

Symbol	Value
$\boldsymbol{p}_V(1)$	$[-3, 9, 0]^\mathsf{T}$ m
$\phi_V(1)$	-30°
$\boldsymbol{p}_T^1$	$[17\,,\ 15\,,\ -6]^\mathsf{T}$ m
$\boldsymbol{p}_T^2$	$[-2\,, -1\,,\ -7]^\mathsf{T}$ m
$\boldsymbol{p}_T^3$	$[\ \ 5\,,\ \ 5\,, -10]^\mathsf{T}$ m
$\boldsymbol{p}_T^4$	$[-9\,, 13\,, -8]^\mathsf{T}$ m
T	1 s
$\boldsymbol{v}_V$	$[3\,, 0\,,\ 0]^\mathsf{T}$ m/s
ω_{max}	30°/s
σ	0.12 m

of n. These values are averaged over all Monte Carlo runs. These values are shown for specific epochs in Table 5.9. Columns of this table present (5.4) of UT $m = 2$, the D-optimal value, and standard deviation in D-optimal value. Rows of this table organize data for different look-ahead duration k at specific epochs.

Again, it can be seen that the expected localization trends hold in general. Discrepancies in the D-optimal value trend may again be ignored considering the magnitude of the standard deviation associated with these values at these epochs (the last column in Table 5.9). The average computational time $\bar{t}_c$ increases from 0.24 s when $k = 1$, to 0.72 s

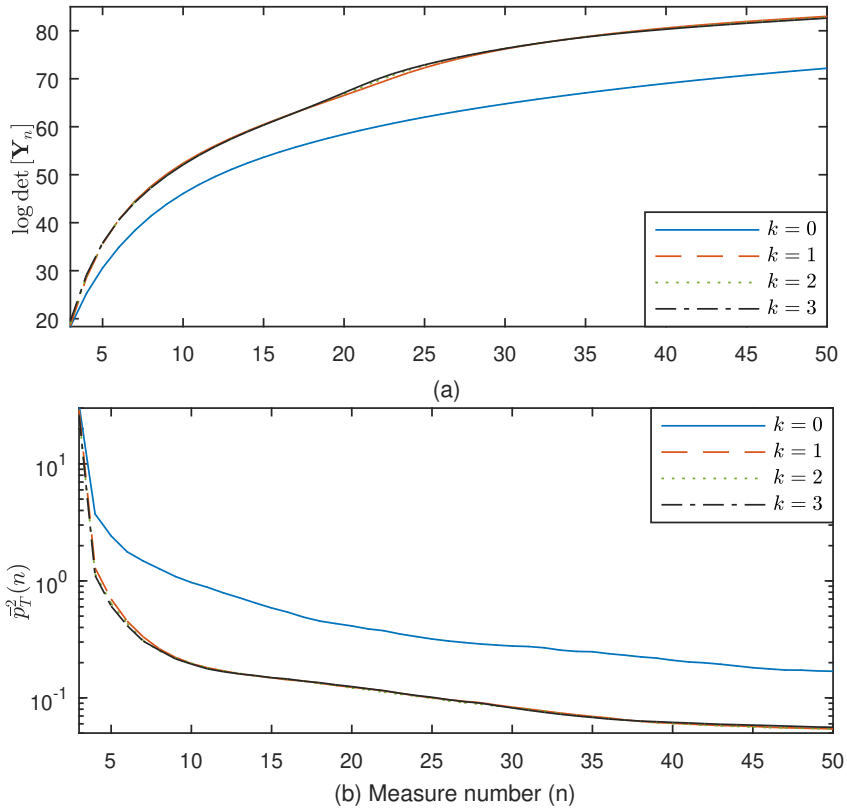

Figure 5.7: Evolution of (a) D-optimal value and (b) localization RMSEE (5.4) as functions of measurement number n for the multiple UT environment. The D-optimal value is averaged over Monte Carlo runs. Sub-figure (b) only displays results for UT $m = 2$, as those for other UTs follow similar trends.

when $k = 2$, to 1.62 s when $k = 3$.

As with the single UT case, the estimator is consistent when applied in an environment with multiple UTs. Fig. 5.8 presents the histogram of (5.3). It is clear that this histogram follows a χ^2_{3M} distribution, indicating that the estimator is consistent.

Fig. 5.9 displays the measurement paths for each value of k during a single Monte Carlo run. The ASV's initial position was $\boldsymbol{p}_V(1) = [-3, 9, 0]^\mathsf{T}$m with yaw angle $\phi_V(1) = -30°$. Note that all optimally planned trajectories tend to orbit around the set of UTs. It is interesting to note the similarity between the trajectories planned using $k = 1$ and $k = 2$,

Table 5.9: MSLA OMLP Multiple UT ($M = 4$) Localization Simulation Results

epoch	k	$\bar{p}_T^{m=2}(n)$[m]	$\log\det[\mathbf{Y}_n]$	$\sigma_{\log\det[\mathbf{Y}_n]}$
$n = 3$	0	32.03	18.36	1.87
	1	28.82	18.59	3.19
	2	25.92	19.08	3.01
	3	26.05	19.54	2.77
$n = 7$	0	1.48	38.38	2.79
	1	0.33	44.47	0.67
	2	0.31	44.34	0.66
	3	0.13	44.23	0.63
$n = 30$	0	0.28	64.76	4.05
	1	0.08	76.19	0.54
	2	0.08	76.31	0.42
	3	0.08	76.30	0.33

and how they differ from that planned with $k = 3$. These trajectories begin to diverge at $n = 30$. From the data in Table 5.9, it can be seen that both (5.4) and D-optimal value are very similar across all $k \geq 1$ (i.e., for all optimally planned ASV trajectories) at this epoch.

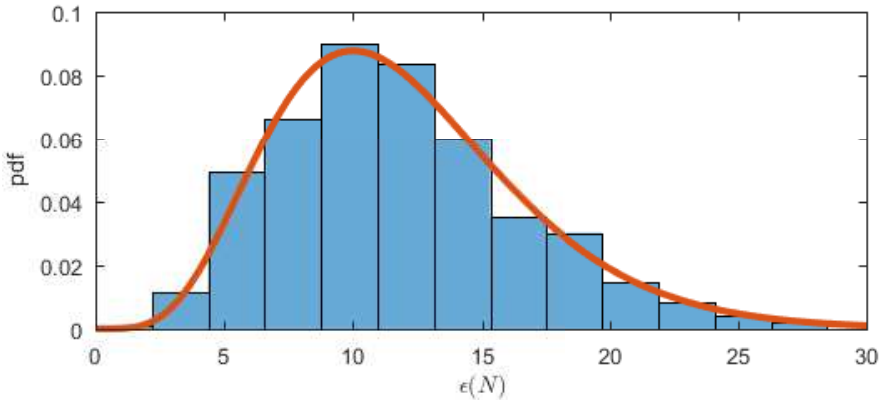

Figure 5.8: Histogram of (5.3) at measurement epoch $n = N = 50$ for all Monte Carlo runs in a multiple ($M = 4$) UT setup. The orange curve displays a χ^2_{12} pdf.

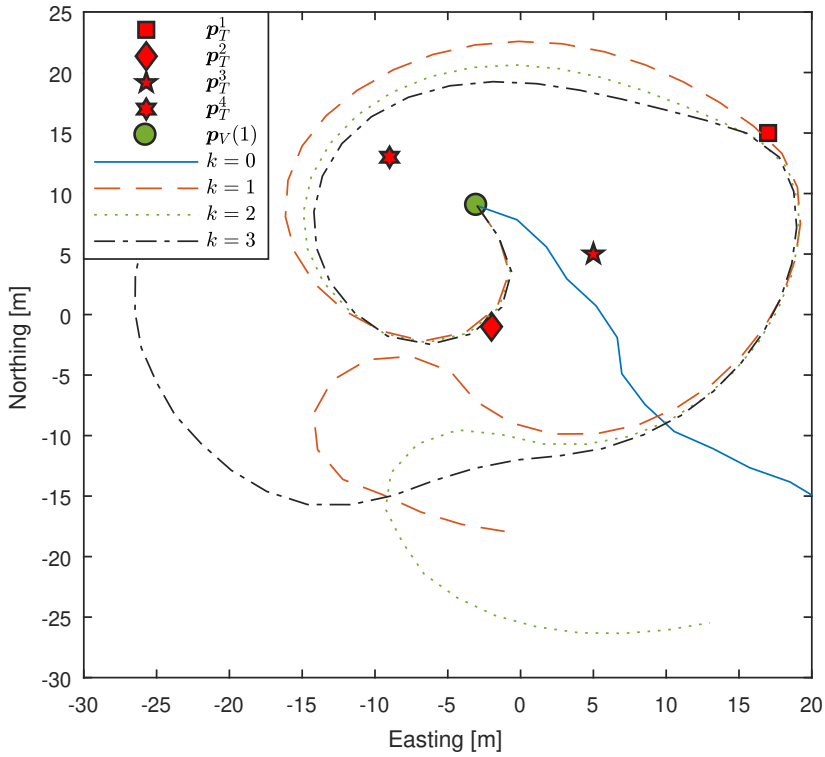

Figure 5.9: Simulated ASV trajectories for various values of k. The initial ASV location is displayed as a green dot with a black outline.

Chapter 6

Experimental Results

This chapter presents experimental results for the UT localization and MSLA OMLP problems. The data collection scheme as well as analysis and description are provided. This chapter will use the same quantitative metrics of localization RMSEE (5.4) and D-optimal value.

6.1 Data collection

Data collection for both single and multiple transponder environments occurred on January 4th, 2018 along pier 169 at SSC Pacific, San Diego, California, USA. Fig. 6.1 illustrates the testing environment. Two SeaTrac x010 acoustic beacons acted as UTs and were fixed to the pier at a depth of 1 m.

A manned surface craft equipped with a SeaTrac x150 USBL beacon and Hemisphere V104^{TM} satellite-based augmentation system (SBAS) GPS Compass maneuvered in the ocean near the pier while ranging to each UT. The GPS receiver computed differen-

Figure 6.1: Top-down view of the the testing area and acoustic ranging locations as measured by the Hemisphere V104^{TM} GPS Compass. The orange dots are locations where USBL range measurements were made from the ASV to the UTs. The green push-pin markers display the configuration of UTs during data collection.

tial GPS (DGPS) position estimates, which were accurate to 1 m. Range data and GPS fixes were acquired at 0.67 Hz and 1 Hz, respectively, and were written to two separate files during data collection. All data was time-stamped with UTC time, which was used to align data in post-processing. Ground truth positions of these UTs were determined by averaging GPS fixes at each UT mounting point over periods of 3 minutes. In this chapter, all positions are represented in a local East, North, Up (ENU) coordinate frame centered at the earliest collected GPS location of the ASV. This point, represented in the geodetic frame, is ${}^{g}\boldsymbol{p}_V = [32.705°\text{N}\,,\ 117.236°\text{W}\,,\ -1.478\text{m}]$.

6.2 Noise Analysis

The maximum likelihood approach:

$$\begin{bmatrix} \hat{r}_i \\ \\ \hat{\sigma}_i \end{bmatrix} = \begin{bmatrix} \frac{1}{N}\sum_{n=1}^{N} r(n) \\ \\ \sqrt{\frac{1}{N-1}\sum_{n=1}^{N} [r(n)-\hat{r}(n)]^2} \end{bmatrix}. \tag{6.1}$$

was used to estimate the range measurement standard deviation using sets of approximately 250 range measurements (i.e., $N = 250$) made while the USBL beacon was stationary. Ground truth ranges of $r_1 = 9.22$m and $r_2 = 2.67$m were determined from GPS position fixes. The evolution of $\hat{r}_i$ and $\hat{\sigma}_i$ are displayed in Fig. 6.2(a)-(b) and Fig. 6.2(c) respectively. The solid red lines of Fig. 6.2(c) display the final estimated range measurement standard deviations $\hat{\sigma}_1 = 62$ mm and $\hat{\sigma}_2 = 113$ mm. Note that $\hat{\sigma}_1$ and $\hat{\sigma}_2$ differ by approximately 50 mm. This difference suggests that measurement noise varies with distance. The maximum of both standard deviation estimates was used as the standard deviation of all measurements for the MAP estimation algorithm (i.e., $\sigma_{USBL} \equiv \max\{\hat{\sigma}_i\} = 113$ mm).

Final estimated range values are displayed in Fig. 6.2(a)-(b) as solid red lines. It is clear that $\hat{r}_1 = 9.02$ m differs from ground truth by 0.2 m, which may be explained by the uncertainty associated with the GPS-derived estimates. To compensate for these errors, one must first return to the models. First, let $\hat{\boldsymbol{p}}_V(n)$ represent the estimate of the ASV location at measurement epoch n as determined via GPS. Additionally, evaluate the Jacobian vector $\boldsymbol{h}^m(n)$ of (3.4) at the measurement location $\hat{\boldsymbol{p}}_V(n)$

$$\boldsymbol{h}^m(n) = \frac{[\hat{\boldsymbol{p}}_T^m(N) - \hat{\boldsymbol{p}}_V(n)]^\mathsf{T}}{\hat{r}^m(n)} \in \mathbb{R}^{1\times 3}. \tag{6.2}$$

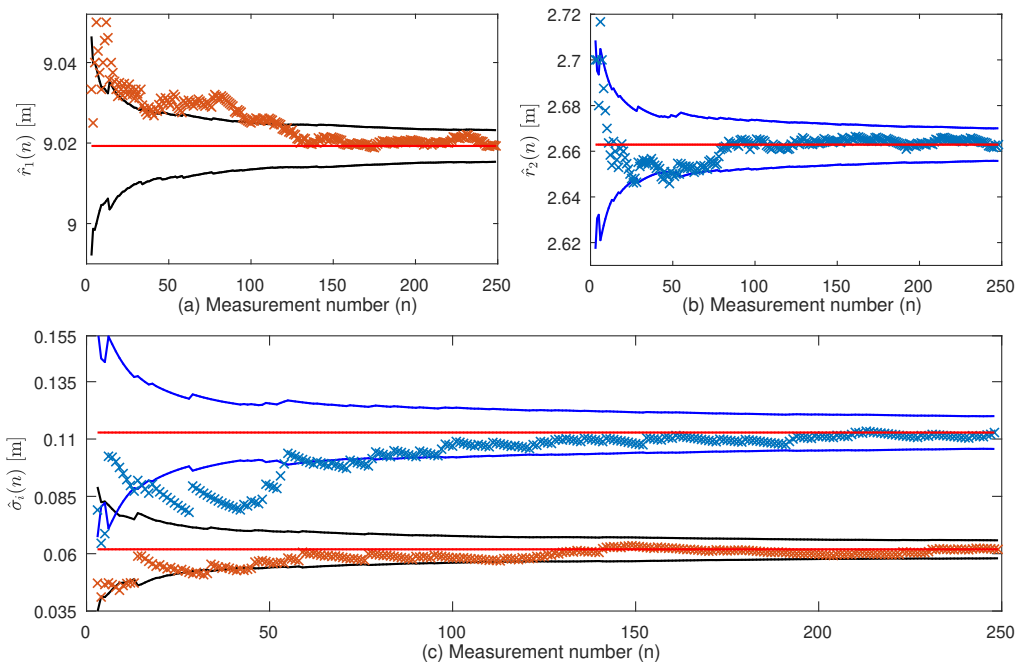

Figure 6.2: (a),(b) Evolution of estimated range between the USBL and each UT using (6.1). (c) Evolution of estimated range measurement standard deviation. Solid red lines denote final estimated values. Blue envelopes denote the standard deviation in these estimates against measurement number.

Recall the model for the USBL range measurement in (2.3). The range can be approximated using a first-order Taylor series expansion around the current estimated UT location and ASV position at the nth measurement epoch (i.e., $\hat{\boldsymbol{p}}_T^m(N)$ and $\hat{\boldsymbol{p}}_V(n)$). Define $\check{r}^m(n)$ (cf. (3.2) as

$$\check{r}^m(n) \triangleq \|\hat{\boldsymbol{p}}_T^m(N) - \hat{\boldsymbol{p}}_V(n)\|_2. \tag{6.3}$$

The approximated range is

$$z^m(n) \approx \check{r}^m(n) + \boldsymbol{h}^m(n)\,[\delta\boldsymbol{p}_T^m - \delta\boldsymbol{p}_V(n)] + w(n), \tag{6.4}$$

where

$$\delta \boldsymbol{p}_T^m \triangleq \hat{\boldsymbol{p}}_T^m(N) - \boldsymbol{p}_T^m(N) \tag{6.5}$$

$$\delta \boldsymbol{p}_V(n) \triangleq \hat{\boldsymbol{p}}_V(n) - \boldsymbol{p}_V(n). \tag{6.6}$$

The residual is defined as

$$\delta z^m(n) \triangleq z^m(n) - \check{r}^m(n) \tag{6.7}$$

$$= \boldsymbol{h}^m(n)\delta \boldsymbol{p}_T^m + w(n) - \boldsymbol{h}^m(n)\delta \boldsymbol{p}_V(n). \tag{6.8}$$

Define $q(n) \triangleq \boldsymbol{h}^m(n)\delta \boldsymbol{p}_V(n)$ as the error due to uncertainty in the GPS solution. The total error in the range measurement is $\epsilon(n) \triangleq w(n) + q(n)$. It is reasonable to assume that $w(n)$ and $q(n)$ are white and are not correlated with each other.

With this in mind, the measurement noise may now be modeled as $\epsilon(n) \sim \mathcal{N}(0, \sigma_\epsilon^2)$, where $\sigma_\epsilon^2 = \sigma_{USBL}^2 + \sigma_{GPS}^2$. The value σ_{GPS}^2 is the variance of $q(n)$. Note that, by construction of $q(n)$, σ_{GPS}^2 is the GPS position error projected onto $\boldsymbol{h}^m(n)$. For purposes of analysis, σ_{GPS} is set to be a constant (i.e., $\sigma_{GPS}^2 = 1\,\mathrm{m}$). With this assumption, the total measurement standard deviation is $\sigma_\epsilon = 1.006\,\mathrm{m}$.

It is worth noting that in some practical applications, the noise covariance matrices may be poorly known and the "luxury" of characterizing them in this manner could be infeasible. To circumvent this issue, adaptive filters could be used [17].

6.3 Processed Results: Evaluation of OMLP (M = 1)

This section evaluates the OMLP strategy in a single UT environment. A Monte Carlo analysis is performed using 100 runs of 50 measurements (i.e., $N = 50$). Constants for

this analysis are provided in Table 6.1. As in Chapter 5, it is expected that the D-optimal value will be larger when ASV locations are determined according to the OMLP strategy.

Table 6.1: OMLP Single UT ($M = 1$) Localization Experimental Settings

Symbol	$\boldsymbol{p}_V(1)$	$\boldsymbol{p}_T$	T	d_{max}	σ_ϵ
Value	$\begin{bmatrix} 8.62 \\ -6.77 \\ 0 \end{bmatrix}$ m	$\begin{bmatrix} 9.21 \\ 1.68 \\ -1.15 \end{bmatrix}$ m	1 s	10 m	1.006 m

Table 6.2 presents the D-optimal value and RMSEE averaged over all Monte Carlo runs for both random and OMLP ASV trajectories. As in the simulated scenarios in Chapter 5.2, the expected data trend holds uniformly.

Table 6.2: OMLP Single UT Localization Experimental Results

epoch	k	$\bar{p}_T(n)$[m]	$\log\det[\mathbf{Y}_n]$	$\sigma_{\log\det[\mathbf{Y}_n]}$
$n = 3$	0	55.11	-3.64	1.14
	1	32.83	-2.82	1.28
$n = 7$	0	26.79	0.21	0.61
	1	17.39	0.89	1.45
$n = 30$	0	16.56	2.71	0.38
	1	3.35	5.65	0.99

6.4 Processed Results: Evaluation of MSLA OMLP (M = 1)

This section evaluates the MSLA OMLP approach presented in Chapter 4.2 for a single UT environment. Again, a Monte Carlo analysis is performed. This analysis consists of 100 Monte Carlo runs. Each run has random initial estimates of transponder locations. An ASV trajectory comprising 50 measurement locations was produced for each run. The initial ASV position is held constant over all runs. Instead of simulating range measurements as was done in Chapter 5.3, this section uses the range measurements collected at SSC Pacific. The experimental settings are tabulated in Table 6.3.

Table 6.3: MSLA OMLP Single UT ($M = 1$) Localization Experimental Settings

Symbol	$\boldsymbol{p}_V(1)$	$\phi_V(1)$	$\boldsymbol{p}_T$	T	$\boldsymbol{v}_V$	ω_{max}	σ_ϵ
Value	$\begin{bmatrix} 8.62 \\ -6.77 \\ 0 \end{bmatrix}$ m	13°	$\begin{bmatrix} 9.21 \\ 1.68 \\ -1.15 \end{bmatrix}$ m	1 s	$\begin{bmatrix} 3 \\ 0 \\ 0 \end{bmatrix}$ m/s	30°/s	1.006 m

Fig. 6.3 presents the D-optimal value and localization RMSEE (5.4). These values are averaged over all Monte Carlo runs. Localization results at specific epochs are given in Table 6.4. This table is organized identically to Table 5.5. Note that, similar to the simulation analysis, one expects that a larger value of k corresponds to better localization accuracy (i.e., smaller values of (5.4). This holds in general; however, discrepancies at all epochs for $k = 2$ can be seen. Similarly, values of (5.4) are significantly larger that those observed in Chapter 5.3. The most likely cause is that the GPS measurement of the UT position is not correct either due to GPS errors or the challenge of placing the GPS receiver

directly above the UT. The average convergence time $\bar{t}_c$ increases from 0.19 s when $k = 1$, to 0.39 s when $k = 2$, to 0.72 s when $k = 3$.

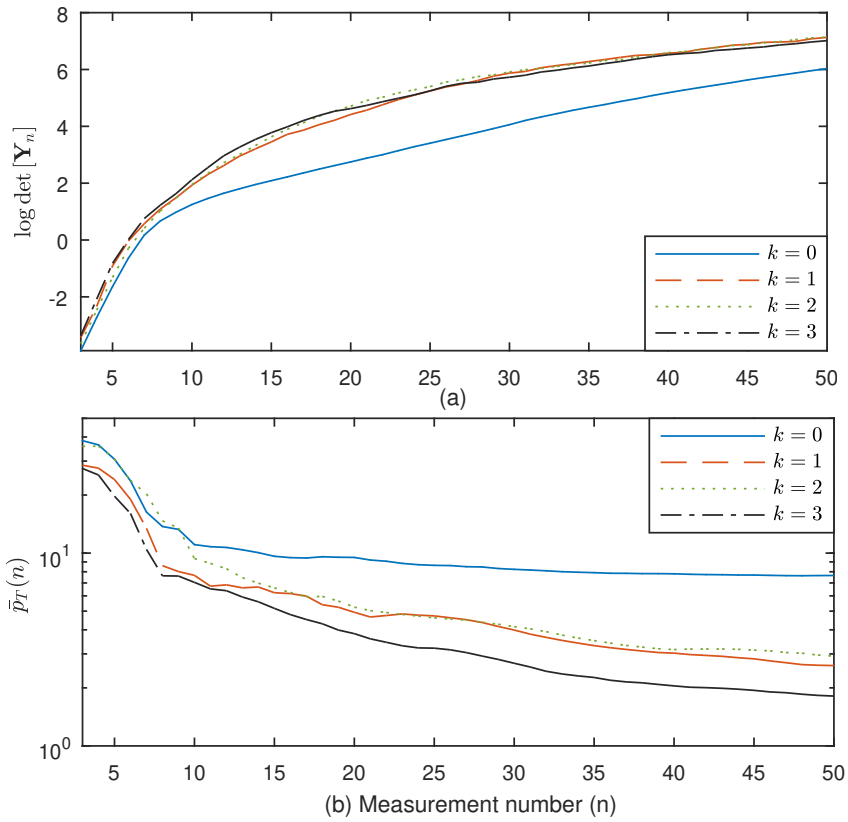

Figure 6.3: Evolution of (a) D-optimal value and (b) localization RMSEE (5.4) as functions of measurement number n for the single UT experimental environment. These values are shown for various values of k.

6.5 Processed Results: Evaluation of OMLP (M = 2)

This section evaluates the OMLP strategy presented in Chapter 4.2 for a multiple UT environment with $M = 2$. A Monte Carlo analysis is performed with the same setup as in Chapter 6.3. The experimental settings are tabulated in Table 6.5.

Table 6.4: MSLA OMLP Single UT Localization Experimental Results

epoch	k	$\bar{p}_T(n)$[m]	$\log\det[\mathbf{Y}_n]$	$\sigma_{\log\det[\mathbf{Y}_n]}$
$n = 3$	0	38.28	-3.89	1.05
	1	28.55	-3.43	1.24
	2	35.78	-3.64	1.33
	3	27.46	-3.36	1.33
$n = 7$	0	16.32	0.17	0.84
	1	13.44	0.57	0.85
	2	20.29	0.42	1.21
	3	10.44	0.78	1.24
$n = 30$	0	8.23	4.08	1.06
	1	3.99	5.87	0.70
	2	4.15	5.91	0.74
	3	2.68	5.73	0.67

Table 6.5: OMLP Multiple UT ($M = 2$) Localization Experimental Settings

Symbol	$\boldsymbol{p}_V(1)$	$\boldsymbol{p}_T^1$	$\boldsymbol{p}_T^2$	T	d_{max}	σ_ϵ
Value	$\begin{bmatrix} 8.62 \\ -6.77 \\ 0 \end{bmatrix}$ m	$\begin{bmatrix} 9.21 \\ 1.68 \\ -1.15 \end{bmatrix}$ m	$\begin{bmatrix} 2.79 \\ 0.44 \\ -1.15 \end{bmatrix}$ m	1 s	10 m	1.006 m

Table 6.6 presents the D-optimal value and RMSEE averaged over all Monte Carlo runs for both random and OMLP ASV trajectories. Again, the expected trend of larger D-optimal value for the OMLP ASV trajectory holds in general. Note that this is not so at epoch $n = 3$. This unexpected result is insignificant considering the magnitude of the standard deviation (i.e., last column of Table 6.6) at this epoch.

Table 6.6: OMLP Multiple UT ($M = 2$) Localization Experimental Results

epoch	k	$\bar{p}_T^{m=1}$[m]	$\log\det[\mathbf{Y}_n]$	$\sigma_{\log\det[\mathbf{Y}_n]}$
$n = 3$	0	53.65	-7.16	2.34
	1	37.45	-8.59	1.45
$n = 7$	0	24.59	0.48	1.43
	1	6.65	3.48	0.46
$n = 30$	0	16.99	5.74	1.11
	1	2.08	10.48	0.89

6.6 Processed Results: Evaluation of MSLA OMLP (M = 2)

This section evaluates the MSLA OMLP approach presented in Chapter 4.2 for a multiple UT environment with $M = 2$. A Monte Carlo analysis is performed with the same setup as in Chapter 6.4. The experimental settings are tabulated in Table 6.7.

Fig. 6.4 presents (5.4) and averaged D-optimal value as functions of measurement epoch. Values at selected epochs are provided in Table 6.8. As in previous cases, unexpected trends in the D-optimal value are insignificant considering the magnitude of the standard

Table 6.7: MSLA OMLP Multiple UT ($M = 2$) Localization Experimental Settings

Symbol	Value
$\boldsymbol{p}_V(1)$	$\begin{bmatrix} 8.62 & -6.77 & 0 \end{bmatrix}^\mathsf{T}$ m
$\phi_V(1)$	13°
$\boldsymbol{p}_T^1$	$\begin{bmatrix} 9.21 & 1.68 & -1.15 \end{bmatrix}^\mathsf{T}$ m
$\boldsymbol{p}_T^2$	$\begin{bmatrix} 2.79 & 0.44 & -1.15 \end{bmatrix}^\mathsf{T}$ m
T	1 s
$\boldsymbol{v}_V$	$\begin{bmatrix} 3 & 0 & 0 \end{bmatrix}^\mathsf{T}$ m/s
ω_{max}	30 °/s
σ_ϵ	1.006 m

deviation associated with these values at these epochs. The values of (5.4) are larger than those in Chapter 5.5. This increase is likely associated with errors in the GPS measurement of the UT locations. The convergence time t_c increases from 0.21 s, to 0.48 s, to 0.99 s for the one-step, two-step, and three-step look-ahead planners, respectively.

Fig. 6.5 demonstrates the measurement paths determined by varying the value of k, along with the randomly planned trajectory, during a single Monte Carlo run. The ASV's initial position is $\boldsymbol{p}_V(1) = [8.62, -6.77, 0]^\mathsf{T}$m with yaw angle $\phi_V(1) = 13°$. As in Chapter 5.5, it can be seen that all optimally planned ASV trajectories orbit around the set of UTs.

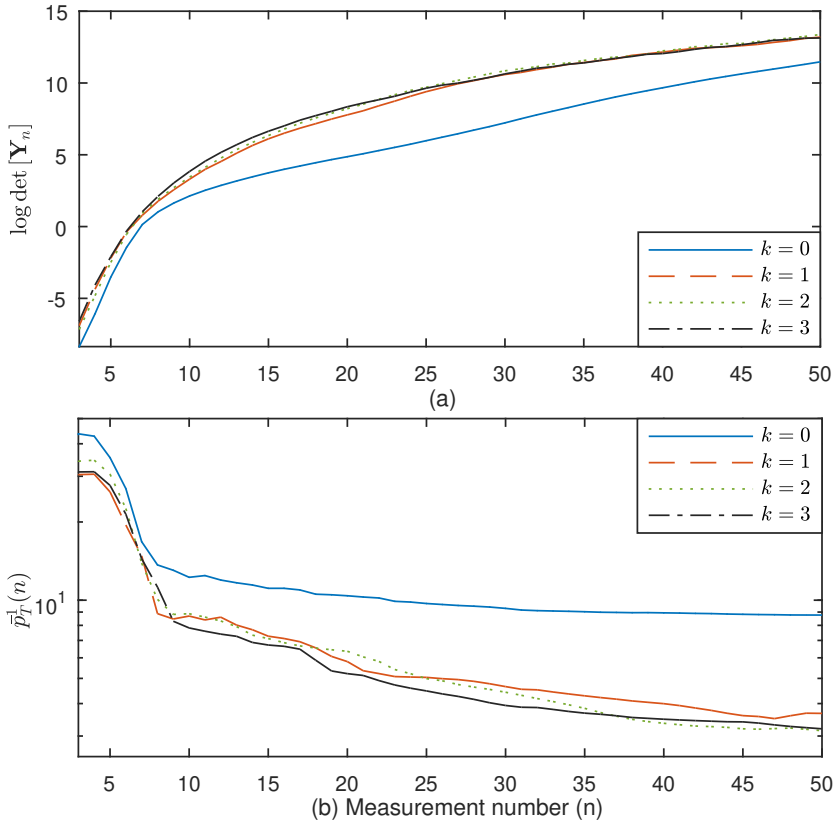

Figure 6.4: Evolution of (a) averaged D-optimal value and (b) localization RMSEE (5.4) as functions of measurement number n for the multiple UT ($M = 2$) experimental environment. These values are shown for various values of k. Note that (b) presents (5.4) for UT $m = 1$ only, as that for UT $m = 2$ is similar.

Table 6.8: MSLA OMLP Multiple UT ($M = 2$) Localization Experimental Results

epoch	k	$\bar{p}_T^{m=1}$[m]	$\log\det[\mathbf{Y}_n]$	$\sigma_{\log\det[\mathbf{Y}_n]}$
$n = 3$	0	43.69	-8.36	1.72
	1	30.43	-6.90	2.06
	2	34.27	-7.16	2.14
	3	31.16	-6.58	2.07
$n = 7$	0	16.79	0.14	0.99
	1	14.81	0.79	1.28
	2	13.89	0.93	1.31
	3	14.43	1.03	1.58
$n = 30$	0	9.29	7.22	1.83
	1	4.65	10.59	1.73
	2	4.42	10.85	1.40
	3	3.93	10.63	1.25

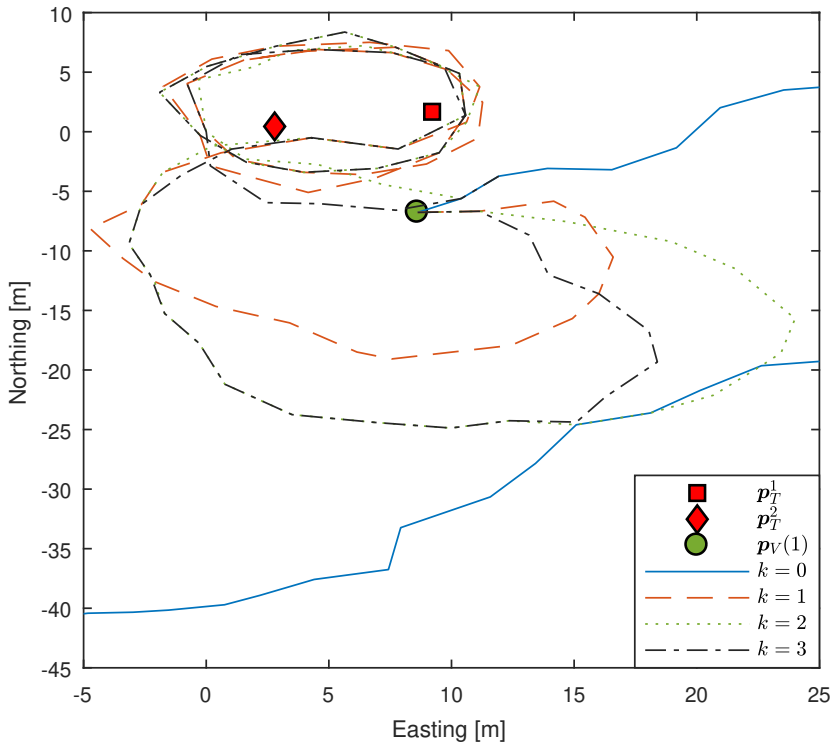

Figure 6.5: ASV trajectories for various values of k using experimental data. UT locations are denoted by red symbols outlined in black. The initial ASV location is displayed as a green dot with a black outline.

Chapter 7

Conclusions

This thesis provided a MAP estimation algorithm for localizing UTs as well as a strategy for the ASV to determine the best future locations at which acoustic ranges must be made to localize the UTs. The simulation results demonstrated the performance of the proposed MAP estimator and the OMLP strategy. The experimental results based on data collected at SSC Pacific demonstrated the performance of the OMLP and MSLA OMLP strategy in an environment containing two UTs. Both simulation and experimental results demonstrated the localization benefit gained by the ASV when planning measurement locations as opposed to randomly choosing measurement locations. Additionally, localization accuracy is shown to increase for larger look-ahead distances at the cost of longer computational cost.

Appendix A

Properties of Matrix Determinants

Consider the block matrix $\mathbf{Q} \in \mathbb{R}^{K \times K}$, constructed as

$$\mathbf{Q} = \begin{bmatrix} \mathbf{A} & \mathbf{B} \\ \mathbf{C} & \mathbf{D} \end{bmatrix}, \tag{A.1}$$

where $\mathbf{A} \in \mathbb{R}^{M \times M}$, $\mathbf{B} \in \mathbb{R}^{M \times N}$, $\mathbf{C} \in \mathbb{R}^{N \times M}$, $\mathbf{D} \in \mathbb{R}^{N \times N}$, and $N = K - M$. When $\mathbf{A}$ and $\mathbf{D}$ are invertible,

$$\det[\mathbf{Q}] = \det[\mathbf{A}] \det\left[\mathbf{D} - \mathbf{C}\mathbf{A}^{-1}\mathbf{B}\right] \tag{A.2}$$

$$= \det[\mathbf{D}] \det\left[\mathbf{A} - \mathbf{B}\mathbf{D}^{-1}\mathbf{C}\right]. \tag{A.3}$$

Now, consider the matrix $\mathbf{Q}'$, constructed as

$$\mathbf{Q}' = \begin{bmatrix} \mathbf{I} & \mathbf{B} \\ -\mathbf{C}^{\mathsf{T}} & \mathbf{I} \end{bmatrix}. \tag{A.4}$$

Using (A.2) and (A.3),

$$\det\left[\mathbf{Q}'\right] = \det[\mathbf{I}] \det\left[\mathbf{I} + \mathbf{C}^{\mathsf{T}}\mathbf{I}^{-1}\mathbf{B}\right] \tag{A.5}$$

$$= \det[\mathbf{I}] \det\left[\mathbf{I} + \mathbf{B}\mathbf{I}^{-1}\mathbf{C}^{\mathsf{T}}\right]. \tag{A.6}$$

From (A.5) and (A.6), it is clear that

$$\det\left[\mathbf{I}+\mathbf{C}^{\mathsf{T}}\mathbf{I}^{-1}\mathbf{B}\right]=\det\left[\mathbf{I}+\mathbf{B}\mathbf{I}^{-1}\mathbf{C}^{\mathsf{T}}\right]. \tag{A.7}$$

Appendix B

Calculation of Confidence Ellipses from Covariance Matrices

One may calculate the confidence ellipse corresponding to the estimate $\hat{\boldsymbol{p}} \in \mathbb{R}^2$ and associated covariance matrix $\mathbf{P} \in \mathbb{R}^{2\times 2}$ as follows [14]. First, find the eigenvalues λ_{min} and λ_{max} and eigenvectors $\boldsymbol{v}_{min}$ and $\boldsymbol{v}_{max} = [x_{max}, y_{max}]$ of $\mathbf{P}$. Define the constants $a \triangleq c\sqrt{\lambda_{max}}$ and $b \triangleq c\sqrt{\lambda_{min}}$, where c is a constant scaling factor corresponding to the desired confidence level of our ellipse. For a confidence level of 95%, $c = 2.4477$. Points along the confidence ellipse are now calculated as

$$\begin{bmatrix} x \\ y \end{bmatrix} = \hat{\boldsymbol{p}} + \mathbf{R}(\phi) \begin{bmatrix} a\cos(\theta) \\ b\sin(\theta) \end{bmatrix}, \quad \forall\, \theta \in [0, 2\pi), \tag{B.1}$$

where

$$\phi \triangleq \texttt{atan2}(y_{max}, x_{max}) \tag{B.2}$$

$$\mathbf{R}(\phi) \triangleq \begin{bmatrix} \cos(\phi) & -\sin(\phi) \\ \sin(\phi) & \cos(\phi) \end{bmatrix}. \tag{B.3}$$

Bibliography

[1] Y. Bar-Shalom, T. Kirubarajan, and X. Li. *Estimation with Applications to Tracking and Navigation*. John Wiley & Sons, Inc., 2002.

[2] P. Batista, C. Silvestre, and P. Oliveira. Single range aided navigation and source localization: Observability and filter design. *Systems & Control Letters*, 60(8):665 – 673, June 2011.

[3] Blueprint Design Engineering Ltd. *SeaTrac Micro-USBL Tracking and Data Modems*, March 2016. Rev. 5.

[4] S. Boyd and L. Vanderbuerghe. *Convex Optimization*. Cambridge University Press, 2004.

[5] V. Djapic, D. Nad, G. Ferri, E. Omerdic, G. Dooly, D. Toal, and Z. Vukić. Novel method for underwater navigation aiding using a companion underwater robot as a guiding platforms. In *Proceedings of IEEE OCEANS Conference*, pages 1–10, June 2013.

[6] M. Dunbabin and R. Lament. Adaptive receding horizon control for a high-speed autonomous surface vehicle in narrow waterways. In *Proceedings of IEEE Conference on Control Technology and Applications*, pages 235–240, August 2017.

[7] M. Ejaz, J. Iqbal, N. Ahsan, and A. Nawaz. Robust geomagnetic aided inertial navigation of underwater vehicles using the ICP algorithm. In *Proceedings of Asia-Pacific Conference on Computational Intelligence and Industrial Applications*, volume 1, pages 257–262, November 2009.

[8] X. Fang, W. Yan, and W. Chen. Sensor placement for underwater source localization with fixed distances. *IEEE Geoscience and Remote Sensing Letters*, 13(9):1379–1383, September 2016.

[9] G. Ferri, A. Munafó, R. Goldhahn, and K. LePage. A non-myopic, receding horizon control strategy for an AUV to track an underwater target in a bistatic sonar scenario. In *Proceedings of IEEE Conference on Decision and Control*, pages 5352–5358, December 2014.

[10] B. Ferriera, A. Matos, H. Campos, and N. Cruz. Localization of a sound source: optimal positioning of sensors carried on autonomous surface vehicles. In *Proceedings of IEEE OCEANS Conference*, pages 1 – 8, September 2013.

[11] J. Garcia, J. Farrell, and Z. Kassas. Optimal measurement location planning for localizing underwater transponders. In *Proceedings of IEEE/ION Position Location and Navigation Symposium*, pages 480–486, April 2018.

[12] J. Garcia, J. Farrell, Z. Kassas, and M. Ouimet. Autonomous surface vehicle measurement location planning for optimal underwater acoustic transponder localization. *IEEE Transactions on Aerospace and Electronic Systems*, 2018. submitted.

[13] F. Hidalgo and T. Brunl. Review of underwater SLAM techniques. In *Proceedings of International Conference on Automation, Robotics and Applications*, pages 306–311, February 2015.

[14] W. Hoover. Algorithms for confidence circles and ellipses. Technical report, US Department of Commerce, National Oceanic and Atmospheric Administration (NOAA), September 1984.

[15] S Huang, N. Kwok, G. Dissanayake, Q. Ha, and G. Fang. Multi-step look-ahead trajectory planning in SLAM: Possibility and necessity. In *Proceedings of IEEE International Conference on Robotics and Automation*, pages 1091–1096, April 2005.

[16] Y. Huang, Y. Zhang, B. Xu, Z. Wu, and J. Chambers. A new adaptive extended kalman filter for cooperative localization. *IEEE Transactions on Aerospace and Electronic Systems*, 54(1):353–368, February 2018.

[17] Y. Huang, Y. Zhang, B. Xu, Z. Wu, and J. A. Chambers. A new adaptive extended Kalman filter for cooperative localization. *IEEE Transactions on Aerospace and Electronic Systems*, 54(1):353–368, 2018.

[18] Z. Kassas and T. Humphreys. Motion planning for optimal information gathering in opportunistic navigation systems. In *Proceedings of AIAA Guidance, Navigation, and Control Conference*, pages 4551 – 4565, August 2013.

[19] Z. Kassas and T. Humphreys. Receding horizon trajectory optimization in opportunistic navigation environments. *IEEE Transactions on Aerospace and Electronic Systems*, 51(2):866–877, April 2015.

[20] Z. Kassas, T. Humphreys, and A. Arapostathis. Greedy motion planning for simultaneous signal landscape mapping and receiver localization. *IEEE Journal of Selected Topics in Signal Processing*, 9(2):246 – 258, March 2015.

[21] Steven Kay. *Fundamentals of Statistical Signal Processing: Estimation Theory*. Prentice Hall PTR, 1993.

[22] J. Khalife and Z. Kassas. Optimal sensor placement for dilution of precision minimization via quadratically constrained fractional programming. *IEEE Transactions on Aerospace and Electronic Systems*, 2018. accepted.

[23] S. Kim, B. Ku, W. Hong, and H. Ko. Performance comparison of target localization for active sonar systems. *IEEE Transactions on Aerospace and Electronic Systems*, 44(4):1371–1380, October 2008.

[24] H. Li, P. Xie, and W. Yan. Receding horizon formation tracking control of constrained underactuated autonomous underwater vehicles. *IEEE Transactions on Industrial Electronics*, 64(6):5004–5013, June 2017.

[25] P. Miller, J. Farrell, Y. Zhao, and V. Djapic. Autonomous underwater vehicle navigation. *IEEE Journal of Oceanic Engineering*, 35(3):663–678, July 2010.

[26] J. Morales and Z. Kassas. Optimal collaborative mapping of terrestrial transmitters: Receiver placement and performance characterization. *IEEE Transactions on Aerospace and Electronic Systems*, 54(2):992–1007, April 2018.

[27] J. Morales, P. Roysdon, and Z. Kassas. Signals of opportunity aided inertial navigation. In *Proceedings of ION GNSS Conference*, pages 1492 – 1501, September 2016.

[28] D. Moreno-Salinas, N. Crasta, M. Ribiero, B. Bayat, A. Pascoal, and J. Aranda. Integrated motion planning, control, and estimation for range-based marine vehicle positioning and target localization. *IFAC Conference on Control Applications in Marine Systems*, 49(23):34 – 40, September 2016.

[29] D. Moreno-Salinas, A. Pascoal, and J. Aranda. Optimal sensor placement for acoustic underwater target positioning with range-only measurements. *IEEE Journal of Oceanic Engineering*, 41(3):620–643, July 2016.

[30] L. Paull, S. Saeedi, M. Seto, and H. Li. AUV navigation and localization: A review. *IEEE Journal of Oceanic Engineering*, 39(1):131–149, January 2014.

[31] J. Perez-Ramirez, D. Borah, and D. Voelz. Optimal 3-D landmark placement for vehicle localization using heterogeneous sensors. *IEEE Transactions on Vehicular Technology*, 62(7):2987–2999, September 2013.

[32] J. Quintas, F. Teixeira, and A. Pascoal. Magnetic signal processing methods with application to geophysical navigation of marine robotic vehicles. In *Proceedings of IEEE OCEANS Conference*, pages 1–8, September 2016.

[33] C. Shen, Y. Shi, and B. Buckham. Integrated path planning and tracking control of an AUV: A unified receding horizon optimization approach. *IEEE/ASME Transactions on Mechatronics*, 22(3):1163–1173, June 2017.

[34] F. Teixeira, J. Quintas, and A. Pascoal. AUV terrain-aided Doppler navigation using complementary filtering. *in Proceedings of IFAC Conference on Maneuvering and Control of Marine Craft*, 45:313 – 318, September 2012.

[35] Francisco Teixeira and António Pascoal. Magnetic navigation and tracking of underwater uehicles. *IFAC Proceedings Volumes*, 46(33):239–244, 2013.

[36] D. Uciński. *Optimal Measurement Methods for Distributed Parameter System Identification*. CRC Press, 2005.

[37] M. Wu and Jian Yao. Adaptive UKF-SLAM based on magnetic gradient inversion method for underwater navigation. In *Proceedings of International Conference on Unmanned Aircraft Systems*, pages 839–843, June 2015.

[38] Z. Kassas and T. Humphreys. Observability analysis of collaborative opportunistic navigation with pseudorange measurements. *IEEE Transactions on Intelligent Transportation Systems*, 15(1):260–273, February 2014.

[39] P. Zhan, D. Casbeer, and A. Swindlehurst. Adaptive mobile sensor positioning for multi-static target tracking. *IEEE Transactions on Aerospace and Electronic Systems*, 46(1):120–132, January 2010.

[40] J. Zhang, C. Shi, K. Tang, and Y. Han. Research and implementation on multi-beacon aided AUV integrated navigation algorithm. In *Proceedings of IEEE OCEANS Conference*, pages 1–5, June 2017.

[41] T. Zhou, D. Peng, C. Xu, W. Zhang, and J. Shen. Adaptive particle filter based on Kullback-Leibler distance for underwater terrain aided navigation with multi-beam sonar. *IET Radar, Sonar Navigation*, 12(4):433–441, 2018.